TITLE PAGE

ARTICLE TITLE*:* VENTRAL HIPPOCAMPAL AND BASOLATERAL AMYGDALAR INPUTS TO DEEP, BUT NOT SUPERFICIAL LAYERS OF MEDIAL PREFRONTAL CORTEX UNDERLIE STRESS SUSCEPTIBILITY

RUNNING TITLE: mPFC Deep Layer Inputs Underlie Stress Susceptibility

Keywords: Medial prefrontal cortex, stress susceptibility, ventral hippocampus, basolateral amygdala, synaptic reorganization, eGRASP

Full names of Authors and their Affiliations:

Sabahaddin Taha Solakoğlu[1], Şefik Evren Erdener[1], Olga Gliko, Alp Can, Uygar Sümbül, Emine Eren-Koçak[1,4,5]

1. Institute of Neurological Sciences and Psychiatry, Hacettepe University, Ankara, Turkey
2. Allen Institute for Brain Science, Seattle, Washington, USA
3. Department of Histology and Embryology, Ankara University Faculty of Medicine, Ankara, Turkey
4. Department of Psychiatry, Faculty of Medicine, Hacettepe University, Ankara, Turkey
5. Lead Contact

Information for Lead Contact:

Mailing Address: Hacettepe Universitesi, Norolojik Bilimler ve Psikiyatri Enstitusu, Tip Fakultesi Binasi, Asma kat, Sihhiye, 06100 / Ankara/ Turkey

Phone number: +90 312 305 2130

Email: erenemi@hacettepe.edu.tr

ABSTRACT

Stress response is essential for adapting to an ever-changing environment. However, the mechanisms that render some individuals susceptible to stress are poorly understood. While chronic stress is known to induce dendritic atrophy and spine loss in medial prefrontal cortex (mPFC), its impact on synapses made by long-range projections terminating on the mPFC remains unknown. Here, we labeled synapses on male mouse mPFC dendrites formed by ventral hippocampus (VH), basolateral amygdala (BLA) and ventral tegmental area (VTA) long-range afferents using different-colored eGRASP constructs. We obtained multispectral 3D images of the mPFC covering all cortical laminae, and automatically segmented the dendrites and synapses. We investigated the relative abundances and spatial organizations of VH-mPFC, BLA-mPFC and VTA-mPFC synapses on a laminar basis in stress naïve, stress resilient and stress susceptible mice. Our findings demonstrate afferent- and lamina-specific differential reorganization of synapses between different stress phenotypes, suggesting specific roles for different long-range projections in mediating the stress response.

GRAPHICAL ABSTRACT

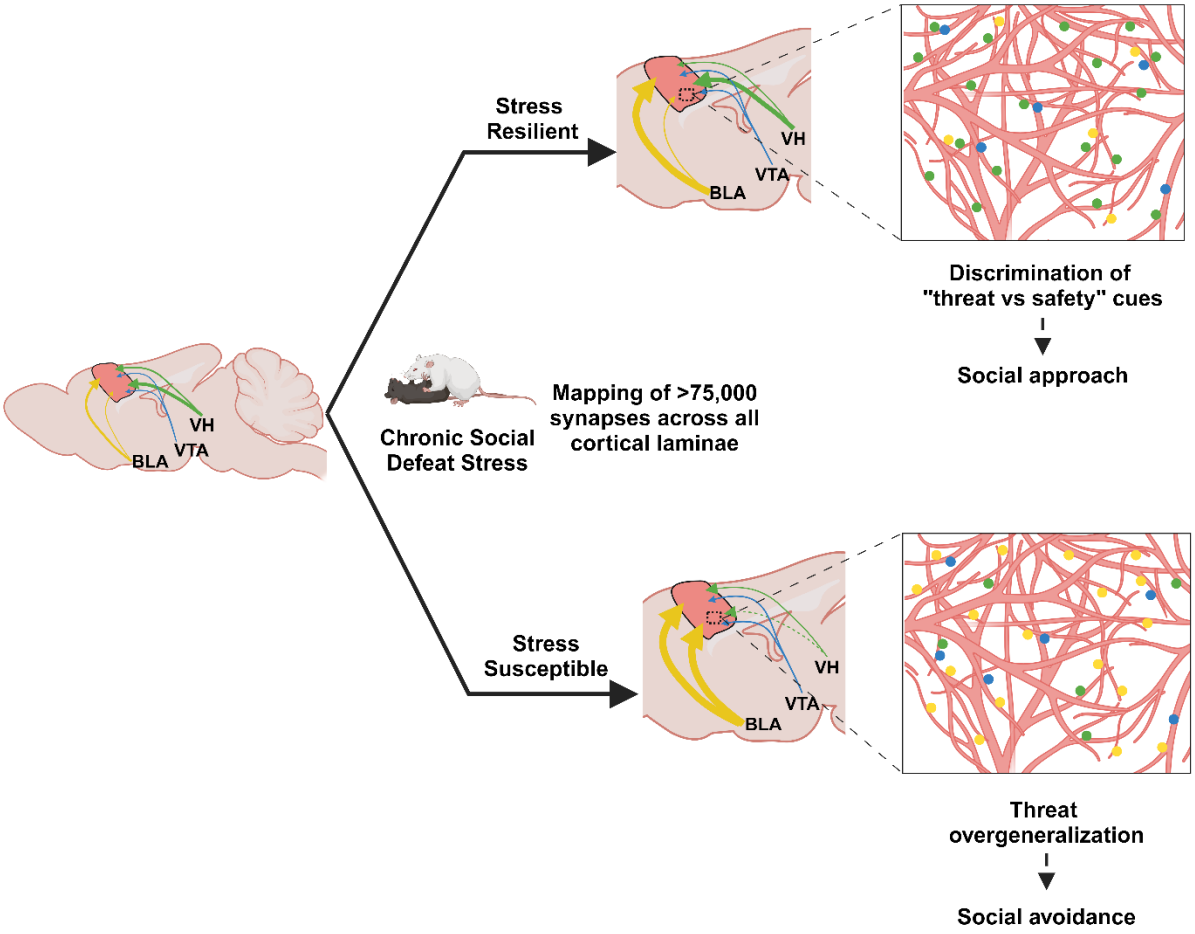

HIGHLIGHTS

- Synapses between mPFC and its long-range BLA, VH and VTA afferents were mapped separately across cortical laminae, and compared among stress naïve, stress resilient and stress susceptible male mice.
- In stress susceptible male mice, there was an increase in the abundance of BLA synapses and a decrease in the abundance of VH synapses within the deep layers of mPFC.
- In stress susceptible male mice, the number of synapses that originate from different brain regions converge onto the same dendritic segment in deep layers of mPFC increased.
- In stress susceptible male mice, the distances between VH and BLA synapses in deep layers of mPFC were altered.
- This laminae- and afferent- specific reorganization of synapses in stress susceptible male mice alter social approach behaviors, presumably by overgeneralizing threat cues.

INTRODUCTION

Stress is an essential adaptive response to imminent or perceived changes in the environment to restore homeostasis. In some individuals, however, stress response can go awry resulting in mental disorders like depression, anxiety disorders and posttraumatic stress disorders for yet unknown reasons. Understanding mechanisms underlying stress susceptibility, therefore, is important for developing prevention and early intervention strategies against stress-related mental disorders.

A key region mediating the stress response is the medial prefrontal cortex (mPFC). Chronic stress causes atrophy of apical dendrites and loss of spines in layer II/III and layer V of mPFC pyramidal neurons without changes in basal dendrites (1-6). These effects of chronic stress are circuit specific: entorhinal cortex-projecting pyramidal neurons show dendritic atrophy in response to chronic stress, whereas basolateral amygdala (BLA)-projecting pyramidal neurons are resilient to stress-induced dendritic remodeling (7). Whether such dendritic resilience to remodeling also applies to afferent projections to the mPFC remains to be answered. Chronic stress-induced dendritic atrophy would be expected to result in the loss of synaptic connections that these dendrites make. If long-range projections to the mPFC from different brain regions are affected differently by this synaptic loss, it will alter the relative weight of inputs from different brain regions on the mPFC and thus, alter the brain circuitry involved in stress response. To date, however, **which mPFC-afferents are affected by dendritic retraction or spine loss is unknown**. Similarly, **whether the reported morphological changes in the dendritic arbor are adaptive or maladaptive remains unknown, because susceptibility to stress was not evaluated in the previous literature**.

mPFC receives input from ventral hippocampus (VH), basolateral amygdala (BLA) and ventral tegmental area (VTA); brain regions indicated in the regulation of the stress response (8, 9). Optogenetic or chemogenetic activation of mPFC or mPFC-projecting VTA, VH and BLA neurons were reported to alter depression- and anxiety-like behaviors (10-19). Unlike sensory cortices, mPFC is agranular, lacks a thalamus projecting layer IV, and receives inputs across all layers (8). Information from various long-range afferents into different layers is integrated by the local circuits within the same layer (intralaminar) or across different layers (interlaminar) to generate an optimal response to adapt to everchanging conditions. **Little is known on how chronic stress alters mPFC circuitry across cortical laminae,** as earlier studies mostly focused on single layers (20). Evidence indicates that long-range inputs may regulate local circuits selectively since they

preferentially target certain cortical layers: Layer II/III and layer V for BLA and VH, respectively (8, 21-23). Distinct mPFC projecting neuron populations identified in both BLA (fear and extinction neurons) and VH (approach and avoidance neurons) regulate stress response and related fear in opposite directions; promoting or suppressing it by integrating the perceptual, emotional and spatial data arriving at mPFC (24, 25). Whether these neurons with opposite functions project to the same or different layers of mPFC is not known. Examining chronic stress-induced changes in specific synaptic inputs across all layers of the mPFC is therefore, crucial to understanding how stress alters brain circuits to produce adaptive responses, as well as what goes awry in stress-related mental disorders.

Here we used the enhanced green fluorescent protein reconstitution across synaptic partners (e-GRASP) system to map synapses between glutamatergic neurons of VH, BLA and VTA and mPFC pyramidal neurons across all layers of the cortical column (26). We obtained multispectral, high resolution 3D images of a ~200 $\times$ 1500 $\times$ 30 μm^3 volume from the mPFC, covering all layers, from stress naïve (SN), stress resilient (SR) and stress susceptible (SS) mice. Mice were divided into SR and SS groups based on their social interaction scores following 10 days of chronic social defeat stress (CSDS). Analysis of the data revealed laminar differences: in superficial layers of mPFC, chronic stress exposure induced similar changes to the relative abundances of BLA-mPFC and VH-mPFC synapses in both SS and SR groups compared to SN mice. In deep layers of mPFC, on the other hand, the abundance of BLA-mPFC synapses relative to all synapses increased, whereas the relative abundance of VH-mPFC synapses relative to all synapses decreased in SS mice compared to SN and SR mice. There were also disruptions to the spatial organization of VH and BLA synapses in deep layers of the mPFC in the SS group. In line with this reorganization of synaptic inputs to mPFC, the percentage of dendritic segments in layer VI that receive input from multiple brain regions was higher in SS mice than the other two groups. Although the percentage of VTA-mPFC synapses was similar across all cortical layers in all groups, we find that the co-presence of a VTA synapse with either BLA or VH synapse on a dendritic segment can predict the stress phenotype. **Our findings reveal an afferent- and lamina-specific differential reorganization of the mPFC synapses in the SS group**. This suggests that disruptions in the long-range afferents to deep mPFC layers may interfere with information processing within the involved circuits, and thereby play a crucial role in mediating the stress response in health and disease.

RESULTS

Labeling and detection of long-range inputs from VH, BLA and VTA to mPFC pyramidal neurons across the cortical column

We used enhanced green fluorescent protein (GFP) reconstitution across synaptic partners (e-GRASP) system in order to differentially label functional synapses between VH, VTA and BLA excitatory projections and mPFC pyramidal neurons (27-29). Briefly, AAVs expressing post-eGRASP were injected into mPFC and AAVs expressing cyan, green and yellow pre-eGRASP were injected into VTA, VH and BLA, respectively (Fig. 1A-C). Three weeks after the injections, mice were exposed to 10-day chronic social defeat stress (CSDS) (Fig. 1D). Stress-naive control mice were kept under similar conditions, but with the cage mates kept on the other side of the plexiglass barrier instead of the aggressor mice. On day 11, stressed animals were divided into stress susceptible (SS) (n=3) and stress resilient (SR) (n=4) groups according to their social interaction ratio scores (SIR) (Fig. 1E-F). Stress naïve (SN) mice (n=3) had SIR scores higher than 1, i.e. spent more time around the cage when a social target was present (Fig. 1F)(30).

Multispectral, high resolution 3D images were acquired from mPFC across the full length of the cortical column (200 x 1500 x 30 μm^3) (Fig. 1G-H) and images obtained were processed according to the pipeline shown in Figure 2, which enabled us to differentially label and quantify all signals in a large 3D volume. Briefly, after stitching the images to form a full-length cortical column, we unmixed the signals with the Learning Unsupervised Means of Spectra (LUMoS) algorithm, since the emission wavelengths of the synaptic signals overlap (Fig. 3A-B, Suppl. Fig. 1, Suppl. Fig. 2) (31). Then, both dendritic and synaptic signals were deconvolved, and dendritic signals were segmented with an artificial neural network model (32) and post-processed to obtain reconstructed dendritic segments (Fig. 3C-F, Suppl. Fig. 1). The Synapse Detector Algorithm (33) was used for detection and quantification of the synapses between VTA, VH and BLA projections and the mPFC pyramidal neuron dendrites, as manual detection of synapses in such a large 3D volume was not practical (Fig. 3G). Reconstructed dendritic tree and synapse locations strongly aligned with their fluorescent signals in 3D (Fig. 3H-I, Suppl. Fig. 1, Suppl. Fig. 3A, Suppl. Vid.1-2,). We confirmed that automated synapse detection is highly accurate by comparing the numbers of detected synapses by the Synapse Detector Algorithm with those annotated manually (Supp. Fig. 4).

The median total numbers of detected synapses were 2,501 (IQR = 1,077 – 6,293; n = 5 cortical columns from 3 mice); 7,509 (IQR = 2,560 – 9,177; n = 5 cortical columns from 4 mice) and 5,845 (IQR = 789 – 8,598; n = 5 cortical columns from 3 mice) in SN, SR and SS mice, respectively. In the SN group, VH-mPFC synapses constituted the highest fraction of all synapses (70.33 ± 16.82%) followed by BLA-mPFC synapses (16.09 ± 11.25%) and VTA-mPFC synapses (13.57 ± 6.09%). In the SR mice, on the other hand, fractions of VH-mPFC and BLA-mPFC were similar (49.62 ± 17.80% and 38.17 ± 20.37%, respectively; p = 0.69, MWU) followed by VTA-mPFC synapses (12.19 ± 4.32%). The percentages of BLA-mPFC, VH-mPFC and VTA-mPFC synapses were similar in SR and SN groups (p = 0.09, p = 0.15 and p = 0.69, MWU, respectively). In the SS group, the percentage of BLA-mPFC synapses tend to be higher than that of VH-mPFC synapses (54.27 ± 17.18% vs. 25.74 ± 15.12%, respectively; p = 0.055, MWU). The percentage of VTA-mPFC synapses in SS mice was similar to that of the other two groups (19.97 ± 9.79%; p = 0.30, MWU).

Layer and stress phenotype-dependent changes to the ratio of BLA synapses

We then examined the distribution of synapses across each cortical layer. Previous literature showed that BLA and VH axonal projections to the mPFC preferentially target layer II/III and layer V, respectively (8, 21-23). In line with the previous literature, we found that the percentage of BLA-to-all detected synapses (BLA/(BLA+VH+VTA)*100) was higher in layer II/III than in layers V and VI in SN group (p = 0.0079, p = 0.035, respectively, MWU test) (Suppl Fig. 3B). Chronic stress exposure increased the percentage of BLA synapses in layer II/III compared to SN controls (p = 0.019, MWU test) (Suppl Fig. 3B,C). The percentage of BLA synapses in layer II/III was similar in SS and SR groups (Fig. 4A-C). On the other hand, the percentage of BLA synapses in layer Vb and VI increased only in the SS group and was significantly higher than those in the SN and SR groups (Fig. 4D,E). The percentage of BLA synapses in layer Vb and VI showed a significant negative correlation with SIR (Fig. 4F-H).

Layer and stress phenotype-dependent changes to the ratio of VH synapses

Changes observed in VH-mPFC synapses were similar to BLA-mPFC synapses but in the opposite direction. Mice exposed to chronic social stress showed a decrease in the percentage of VH-to-all synapses [VH/(BLA+VH+VTA)*100] in layer II/III compared to SN controls (p=0.019, MWU test) (Suppl Fig. 3B,D). We did not observe any differences in the percentage of VH synapses between SS and SR groups (Fig. 4I-K). In contrast, only SS mice showed a significantly

decreased percentage of VH synapses in layer Vb and VI (Fig. 4L-M). The percentages of VH synapses in layer Vb and VI were significantly correlated with SIR (Fig. 4N-P).

Invariance of the ratio of VTA synapses to the stress phenotype

The VTA-to-all synapses percentage (VTA/(BLA+VH+VTA)*100), was similar across all layers of the mPFC in all groups (Fig. 4Q-U, Suppl. Fig. 3B,E). We did not find statistically significant correlations between SIR and the percentages of VTA synapses across different layers (Fig. 4V-X).

A low dimensional representation of the relative abundances of VH, BLA and VTA synapses across the cortical column visually differentiates SS mice from SR mice.

To further examine the dissociation of groups according to their stress susceptibility, we examined the low-dimensional structure of synaptic distributions across all layers using principal components analysis (PCA) in 13 cortical columns with an intact layer I (2 columns lacking layer I were excluded from the analysis, due to damage resulting in 13 columns, presumably from the AAV injections). We converted the 3x13x5 (synapse type count x column count x layer count) synapse percentage matrix into a 13x15 matrix by arranging the synaptic percentage data from VTA, VH and BLA from each layer into a single row. We then applied PCA to this matrix and visualized the distribution of cortical columns in the 2-dimensional plane based on the top two principal components (PCs). Approximately 77.44% of the variance in the synaptic percentages across the cortical column was captured by these two PCs. Notably, the cortical columns associated with stress susceptibility occupied distinct locations in this low dimensional space (Fig. 4Y). This supports the finding that relative synaptic abundances of BLA, VH and VTA across the mPFC laminae can explain the behavioral differences between SR and SS mice.

The abundance of dendritic segments receiving input from multiple brain regions increases in SS mice.

To gain a deeper insight into differences of SS mice from others, we investigated the percentage of reconstructed dendritic segments that have 2 or more synapses in layer Vb and VI (Fig. 5, Suppl. Fig. 5). In both layer Vb and layer VI, the percentage of dendritic segments receiving input from only VH was significantly lower and those receiving input from only BLA tended to be higher in the SS mice than the other two groups. There was no difference in the percentage of dendritic segments receiving input from only VTA among groups (Suppl. Fig. 5).

In layer Vb, the percentage of dendritic segments receiving input from multiple brain regions was similar between groups (Fig. 5A-C). When analyzed separately for each pair of multi-brain region originated synapses on individual dendritic segments, however, we observed that the percentage of BLA&VTA synapses increased in both stressed groups; the rise in the SS group was significantly higher than that of the SR group (Fig. 5D-E). In layer VI, on the other hand, the percentage of dendritic segments receiving input from multiple brain regions was significantly higher in the SS group than the other two groups (Fig. 5F-H). When analyzed separately for each pair, we observed a reduction in the percentages of VTA&VH synapses on the same dendritic segment in the SS group (Fig. 5I-J). Interestingly, we did not observe any difference in the percentage of BLA&VH synapses on the same dendritic segment among groups in either layer Vb or layer VI (Fig. 5E,J).

These findings suggest that under physiological conditions (i.e. in case of an adaptive stress response) stress response alters synapses in deep layers by changing the number of synapses originating from the same brain region on a single mPFC dendritic segment, and that increases in the percentage of multi-origin-synaptic pairs on the same dendritic segment in SS mice may cause a disorganization in the outputs of these layers.

The spatial organization of VH and BLA synapses on mPFC deep layers is disrupted in SS mice.

To elucidate whether there is a general innervation pattern of the mPFC by VH and BLA in layer Vb and VI, we measured the Euclidean distances between VH and BLA synapses and determined the nearest VH and BLA synapses for each VH and BLA synapse in the reconstructed ~200 x 700 x 30 μm^3 mPFC volume. Among the three groups studied, there were no differences in either the distances of VH synapses to their corresponding closest VH synapses or the distances of BLA synapses to their corresponding closest BLA synapses (Fig. 6A-B). We observed differential spatial organization of VH and BLA synapses relative to each other in SN/SR mice vs. SS mice: In the SN and SR mice, the distances of VH synapses to their corresponding nearest BLA synapses were distributed relatively uniformly across a wide range (Fig. 6C), whereas the BLA synapses were preferentially located in close proximity (within 5 um) to VH synapses (Fig. 6D). In contrast, in the SS group, we observed a statistically significant decrease in the distances of VH synapses to their corresponding closest BLA synapses and a statistically significant increase in the distances of BLA synapses to their corresponding closest VH synapses (Fig. 6C-D).

These results suggest that the long-range projections follow structured, differential innervation patterns and are not random (Fig. 6E-F). We quantified this observation by training a random forest classifier (RFC) on a 42,317 x 8 matrix of nearest synaptic distances, where each row corresponds to a synapse. In each row, the first four columns denote the Euclidean distances of that synapse to its four closest VH synapses, and the last four columns denote the distances to its four closest BLA synapses. This RFC had 76% accuracy in differentiating all three groups (Fig. 6G). Examining the confusion matrix reveals that the RFC can predict the SS group with ~88% accuracy and the SR group with ~83% accuracy. However, the prediction accuracy of the SN group is low (~47%) (Fig. 6H). We observed that the classification accuracy and the F1 score (harmonic mean of precision and recall) decreases significantly when the RFC is trained on the same dataset with shuffled labels, simulating a scenario where synapses from the different regions are randomly distributed in the mPFC over the observed synaptic locations (Fig. 6G-J). Finally, we visualized this result using uniform manifold approximation and projection (UMAP) (34), a non-linear dimensionality reduction method: the synapses associated with the SR and SS phenotypes occupy different regions of the two-dimensional UMAP map of the same data matrix (Fig. 6K-L).

DISCUSSION

While the stress response is a fundamental component of the behavioral repertoire of animals, a mechanistic, circuit-level understanding of it in health and disease remains incomplete. This is, in part, due to the complexity of the distributed circuitry that governs the behavioral responses, involving numerous synaptic connections between multiple brain regions. Here, by using multiple eGRASP constructs, multispectral volumetric imaging, computational tools for dendrite and synapse identification, and statistical methods for analyzing the resulting large-scale dataset, we aimed to elucidate this circuitry in the mouse. To our knowledge, this is the first study that mapped VH-mPFC, VTA-mPFC and BLA-mPFC synaptic connections separately across all cortical layers and compared them between SN, SS and SR mice. This multi-pronged approach revealed distinct patterns of organization of synaptic inputs to deep and superficial mPFC layers in the stress response and susceptibility.

Previous literature showed that BLA projections preferentially target layer II (21, 22, 35), whereas, VH projections are largely restricted to layer V of mPFC (22, 23). Consistent with these findings, we observed a similar organization of long-range synaptic inputs to the cortical layers of SN mice. CSDS altered the ratios of BLA-to-all synaptic inputs [BLA/(BLA+VH+VTA) and VH-to-all synaptic inputs [VH/(BLA+VH+VTA)] in mPFC superficial layers, regardless of stress susceptibility of the mice. Organization of long-range inputs to deep layers of mPFC, on the other hand, was disrupted only in the SS group: BLA-mPFC synapses predominated over VH-mPFC synapses in layer Vb and VI suggesting that the reorganization of long-range synaptic inputs to mPFC deep layers may underlie stress susceptibility. In contrast, the ratio of VTA-to all synaptic inputs [VTA/(BLA+VH+VTA)] was similar across all cortical layers and groups.

All mice exposed to CSDS showed an increase in the abundance of BLA-mPFC synapses and a reduction in the abundance of VH-mPFC synapses in layer II/III, indicating that changes observed in this layer are related to stress exposure rather than stress susceptibility. Previous studies reported reductions in dendritic length and spine numbers in mPFC layer II/III after chronic stress exposure (1-5). Our results, when considered together with these findings, suggest that mPFC neurons that receive input from VH were preferentially atrophied by chronic stress resulting in a decrease in VH inputs, whereas those that receive input from BLA were unaffected. Supporting this suggestion, Shansky et al (2009) demonstrated that pyramidal neurons projecting to entorhinal cortex showed dendritic atrophy in response to chronic stress, whereas those projecting to amygdala were resilient to stress-induced dendritic remodeling (7). Considering that

there is a reciprocal connection between BLA and mPFC (i.e. BLA inputs preferentially innervate BLA-projecting mPFC neurons), one may speculate that BLA input receiving mPFC neurons are also resilient to atrophy (21, 22, 35, 36).

Brain networks connecting mPFC, BLA, and hippocampus are involved in the regulation of fear-related and social behaviors(14, 17, 37-40). The interplay between these three regions in the control of anxiogenic/social behaviors is complex, and may both promote and suppress fear or social behavior (17, 22, 24, 36, 41). Input from BLA and VH to the mPFC were reported to have opposite effects on fear-related and social behaviors(14, 17, 42). Moreover, studies have demonstrated that within each of these brain regions there are distinct populations of neurons with distinct connections that encode “safe” and “aversive” cues. This allows the organism to react optimally to various stimuli (24, 25, 36). Selective activation of distinct neuronal circuits may serve as a mechanism to switch between alternative behavioral responses by integrating sensory, contextual and emotional information, fine-tuning the expression and suppression of fear-related and social responses (24, 41, 43).

Mice are social animals and they tend to spend more time with social targets (stranger mouse) compared to non-social targets (i.e. objects) (44). Following CSDS, SS and SR mice demonstrate opposite behavioral responses when encountering a novel mouse in a novel context: SS mice exhibit social avoidance, while SR mice demonstrate social approach. This suggests that SR mice can discriminate threat-related stimuli or contexts from novel stimuli or contexts, whereas SS mice tend to overgeneralize the threat to all novel stimuli or contexts they encounter. Overgeneralization of fear is a characteristic feature of anxiety disorders, and thought to be one of the mechanisms underlying posttraumatic stress disorder, panic disorder and generalized anxiety disorder (45-48). The increase in the relative abundance of long-range inputs from BLA and the decrease in the relative abundance of long-range inputs from VH to deep layers of the mPFC pyramidal neurons in SS mice, as reported in the current study, could potentially interfere with the discrimination between threat-associated and non-threat associated stimuli. This interference may then disrupt the ability of the mPFC to produce an adaptive response. Intriguingly, a previous study showed that the discrimination of aversive cues from safe cues was associated with synchrony between mPFC and BLA activities in the theta frequency range (41). The entrainment of BLA activity by mPFC activity in the theta frequency range was reported in only those mice that can discriminate conditioned auditory tones from unconditioned tones (discriminators). Specifically, these mice demonstrated a significantly higher degree of freezing in response to conditioned auditory tones compared to unconditioned tones (41). Additionally, the

VH also synchronizes with mPFC activity at the theta frequency range during the exploration of anxiogenic novel environments, facilitating the discrimination of safe and aversive components of the environment (18, 19, 43). VH is also implicated in the formation and storage of social memory (39). VH neurons are more strongly activated in response to a familiar mouse compared to a stranger mouse, and their optogenetic inhibition interferes with the discrimination of familiar and unfamiliar mice (39). In parallel with these findings, our results suggest that the balance between BLA and VH inputs to the mPFC is crucial in associating social cues with aversion, and in discriminating safe cues from aversive cues to produce an adaptive response (Please see graphical abstract). As we did not investigate the efferent connections of mPFC, it remains unclear which brain region is impacted by the reported disorganization of long-range inputs to deep layers of mPFC. However, existing literature indicated the involvement of mPFC projections to nucleus accumbens (NAc) in social approach behavior (49). Considering that the organization of long-range inputs in SS mice was impaired only in the deep layers of the mPFC, which predominantly project to subcortical regions, it is possible that imbalance in BLA and VH inputs to mPFC deep layers may disrupt the activity in mPFC-NAc circuit. This issue warrants further investigation in future studies.

How excitatory inputs from different brain regions onto mPFC contribute to different stress phenotypes is an intriguing question. One possibility is that these inputs may selectively target specific neuronal ensembles, each with distinct roles in fear-related behavior. Supporting this suggestion, our findings showed that inputs from the same brain region tend to make synapses on the same dendritic segments in SN and SR mice. In SS mice, however, we observed increase in the number of inputs from different brain regions converging onto the same dendritic segment. Additionally, our data indicates that under normal physiological conditions, inputs from the BLA tend to terminate in close proximity to VH inputs, but it appears crucial for some VH-mPFC synapses to be located farther from BLA-mPFC synapses. In SS mice, this innervation pattern is disrupted with almost all VH inputs terminating close to BLA-inputs. One may speculate that proximity of BLA inputs to VH inputs play a role in integrating threat-signals into ongoing information processing within those neuronal ensembles, while VH inputs distant from BLA inputs may be involved in processing non-threat-related information. Whether these distinct inputs originate from distinct mPFC-projecting VH neuronal populations, each with opposite roles on fear-related behaviors, remains to be addressed in future studies (25). Interestingly the disorganization in VH-BLA innervation of deep mPFC layers was not observed at the level of

single dendritic segments, as there were no differences in the percentage of VH-BLA inputs on single dendritic segments among all three groups.

Most of the earlier studies on the role of VTA on stress response that focused on dopaminergic neurons have indicated the role of VTA in regulating both stress response and social behavior. Although we did not observe any changes in the ratio of VTA-to-total synaptic inputs either following stress exposure or as a result of stress susceptibility, we observed that in dendritic segments receiving input from multiple brain regions, change in VTA input-containing synaptic pairs correlated with stress susceptibility. This suggests that VTA inputs also play a role in the regulation of stress response.

Our study primarily focused on long-range projections to pyramidal mPFC neurons, and we did not investigate projections terminating on mPFC interneurons. This decision was influenced by the challenges associated with confocal multicolor imaging, particularly the quantitative limit for visualizing multiple fluorophores simultaneously. Given various reports of altered excitatory:inhibitory balance in stress-related mental disorders long-range projections on mPFC interneurons may also contribute to fine-tuning the stress response (50-54). To provide a more comprehensive understanding of the neural circuitry underlying stress response and resilience, investigation of the role of long-range projections to mPFC interneurons is warranted in future studies.

Our study was conducted only in male mice, thereby restricting the generalizability of our findings to females. CSDS is generally used in identification of stress susceptibility in male mice due to challenges in implementing it in females. Resident mice of either sex do not attack the intruder females, so, unlike male mice, females do not naturally face such social attacks. Although a CSDS paradigm has been developed to induce social defeat in females by applying another CD1 male mouse's urine to vaginal orifices of female intruders (55), we chose to conduct our study in male mice to explore the mechanisms underlying stress susceptibility and resilience, given its higher ethological validity in males.

The computational tools that enable the large-scale 3D synaptic study pursued here have some limitations. While automated tracing of dendrites broadly succeeds, it can introduce mistakes, especially by linking segments that belong to different neurons (32). We addressed it by using a higher threshold for segmentation. However, this resulted in shorter segments, affecting the calculation of dendritic path distances (e.g., to the nearest synapses). Therefore, instead, we

focused on the Euclidean distances between synapses. Not only is this calculation very robust, but it also provides information about the 3D spatial organization of VH-mPFC, VTA-mPFC, and BLA-mPFC synapses across a column of mPFC.

In conclusion, the findings of the current study enhance our comprehension of chronic stress effects on brain circuitry in both physiological and pathological states by focusing on the synapses formed by long-range projections on mPFC. We have demonstrated laminae- and afferent-specific changes in stressed groups depending on their stress phenotype (resilient vs susceptible), highlighting potential avenues for developing preventive or therapeutic strategies in stress susceptible individuals following a stressful or traumatic event.

METHODS

Key resources table

REAGENT or RESOURCE	SOURCE	IDENTIFIER
Bacterial and virus strains		
AAV2/1-CWB-pre-eGRASP(p32)	Charite – Universtatmedizin Berlin Viral Core Facility	#VCA-340a
AAV2/1-EWB-DIO-myrTagRFP-T-P2A-post-eGRASP	Charite – Universtatmedizin Berlin Viral Core Facility	#VCA-338a
AAV2/1-CWB-cyan pre-eGRASP(p30)	Charite – Universtatmedizin Berlin Viral Core Facility	#VCA-339a
AAV2/1-CWB-yellow pre-eGRASP(p32)	Charite – Universtatmedizin Berlin Viral Core Facility	#VCA-337a
AAV2/1 – CaMKIIα - iCre	Charite – Universtatmedizin Berlin Viral Core Facility	#BA-257b
Critical commercial assays		
QIAGEN Plasmid Mega Kit	Qiagen	Cat. #12181; RRID:SCR_008539
Experimental models: Organisms/strains		
C57BL/6	Hacettepe University Laboratory Animals Research and Application Centre (HUDHAM)	N/A
CD-1	Kobay Deney Hayvanları Laboratuvarı	N/A
Recombinant DNA		
pAAV-CWB-pre-eGRASP(p32)	Choi et al.(26)	Addgene #111598; RRID:Addgene_111598
pAAV-EWB-DIO-myrTagRFP-T-P2A-post-eGRASP	Choi et al.(26)	Addgene #111581; RRID:Addgene_111581
pAAV-CWB-cyan pre-eGRASP(p30)	Choi et al.(26)	Addgene #111586; RRID:Addgene_111586
pAAV-CWB-yellow pre-eGRASP(p32)	Choi et. al.(26)	Addgene #111580; RRID:Addgene_111580
Software and algorithms		

Fiji is just ImageJ 2.1	Schendelin et al.(56)	https://fiji.sc
Vaa3D – x 1.1.2	Peng et al.(57)	https://github.com/Vaa3D; RRID:SCR_002609
BigStitcher	Hörl et al.(58)	
ZEN 3.2 Black Edition	Zeiss	https://www.zeiss.com/
LUMoS	McRae et al.(31)	https://imagej.net/plugins/lumos-spectral-unmixing
RedLionfish (RL) deconvolution	Perdigao et al.(59)	https://github.com/rosalindfranklininstitute/RedLionfish
Neuron Reconstruction Algorithm	Gliko et. al.(32)	N/A
IS Detector (Synapse Detector)	Iascone et al(33)	https://github.com/Vaa3D
Other		
LSM810 laser-scanning confocal microscope	Zeiss	https://www.zeiss.com/
Leica SP8 confocal microscope	Leica	https://www.leica-microsystems.com/
Allen Brain Atlas	Allen Institute for Brain Science	http://mouse.brain-map.org

Animals

Ten 12–16-week-old male C57BL/6 wild-type and 4–20-month-old CD-1 male wild-type mice were used for the study. Mice were maintained at 12:12 light:dark cycle (07:00-19:00) and stable temperature (19-22 ^{o}C) with *ad libitum* access to food and water. Mice were purchased from Kobay AS and Hacettepe University Laboratory Animals Research and Application Centre, and housed at the Animal Unit of the Institute of Neurological Sciences and Psychiatry during the experiments. All procedures were done in accordance with Animal Experimentations Local Ethics Board of Hacettepe University (Ethics number: 2019/78).

Enhanced GFP (green fluorescent protein) Reconstitution Across Synaptic Partners (e-GRASP) system and Construction of Adeno Associated Virus

e-GRASP system allows to visualize functional synapses based on complementation of pre-synaptic neurexin and post-synaptic neuroligin, each of these proteins are fused with 2 complementary split GFP fragments so that binding of neurexin to neuroligin results in GFP reconstitution without dramatically changing their binding affinities (27-29, 60).

eGRASP plasmids to label synaptic connections from 3 different brain regions onto mPFC dendritic tree; specifically, pAAV-CWB-yellow-pre-eGRASP(p32), pAAV-CWB-cyan-pre-eGRASP(p30), pAAV-CWB-green-pre-eGRASP(p32), pAAV-EWB-DIO-myrTagRFP-T-P2A-post-eGRASP were obtained from Addgene (#111580, #111581, #111586, #111598, gifts from Dr. Bong-Kiun Kaang)(26). Plasmids were purified by Qiagen Plasmid Mega kit and then sent to Viral Core Facility of Universtatmedizin Berlin Charite to be packaged into AAV 2/1. AAV2/1-CaMKIIα-iCre was obtained from the same facility.

Intracranial Virus Injections

Mice were anesthetized with intraperitoneal (ip) injection of 5-10 mg/kg xylazine and 50-100 mg/kg ketamine, then maintained under 1-2% isoflurane or sevoflurane anesthesia. AAV2/1-pAAV-CWB-yellow-pre-eGRASP(p32), AAV2/1-pAAV-CWB-green-pre-eGRASP(p32) and AAV2/1-pAAV-CWB-cyan-pre-eGRASP(p30) were injected into BLA, VH and VTA, respectively. AAV2/1-CaMKIIα-iCre and AAV2/1-pAAV-EWB-DIO-myrTagRFP-T-P2A-post-eGRASP were injected into mPFC. Injections were performed by lowering 28-gauge microinjectors unilaterally into right VH, VTA, BLA and mPFC sequentially (coordinates from bregma are AP: -1.2, ML: -3.42, DV: -5.4 **for BLA**; AP: +1.3, ML: -0.3, DV: -2.3 **for mPFC**; AP: -3.05, ML: -3.35, DV: -4.2 **for VH** and AP: -2.87, ML: -0.35, DV: -5.1 **for VTA**). AAV2/1 injections were carried out at a rate of 0.1 µL/min, details of viral genome densities and volumes injected in each region are summarized in Supplemental Table-1. Microinjectors were kept in the injection sites for 10 minutes to allow the diffusion of AAVs. Craniotomies were then filled with bone wax; scalp was sutured and subcutenous flunixin meglumine (2.5 mg/kg) and ip saline (0.3 ml) was administered. Eye ointment was frequently applied and rectal temperature was monitored during the procedure.

Experimental Timeline

After AAV2/1 injections, stress exposed mice were left undisturbed for 3 weeks to allow for optimal expression of the virus. After 10-day chronic social defat stress (CSDS), social interaction (SI) test was performed to determine stress phenotype (susceptible vs resilient). Stress-naïve mice were kept under similar conditions for 4 weeks except with another C57BL/6 mice separated by a plexiglass barrier. After the SI test (within ~ 1h), the brains were removed for processing.

Chronic Social Defat Stress and Social Interaction Test

Chronic Social Defat Stress (CSDS) was carried out as Golden et al described (30). Briefly, an intruder C57BL/6 male mouse was placed in the cage of an aggressive CD-1 mouse. Duration of physical interaction was determined with an algorithm for each mouse based on the occurrence of bleeding to prevent injury. Then the C57BL/6 mouse was physically separated from the CD1 mouse by dividing the cage with a plexiglass barrier that allowed for visual, olfactory and vocal interaction. They were housed in the divided cage for 24 hours, then the stress protocol was repeated for 10 days with a different CD-1 mice. On the 11th day social interaction test (SI test) was carried out. Briefly, the interaction time of C57BL/6 mice with an interaction cage (9.5 cm in diameter) placed at one edge of a 45 x 45 cm arena was recorded with Ethovision XT 8.0. The SI Test consisted of two stages. During the first stage, mice explored the arena that contains an empty interaction cage for 5 minutes. During the second stage, an unfamiliar novel CD-1 male mouse was put in the interaction cage and C57BL/6 mice explored the same arena for 5 minutes.

The interaction zone was defined as the circular area with a 23.75 cm diameter sharing the same center with interaction cage. Social interaction ratio was calculated by dividing the time spent around the interaction cage when CD-1 mouse was present to the time spent around the interaction cage when interaction cage was empty. Mice were classified as stress-resilient if the SI ratio is above 1 and stress-susceptible if the SI ratio is below 1.

Tissue Preparation

After the SI test, mice were anesthetized with %10 chloral hydrate-saline solution and perfused with heparin and 4% PFA. Brains were extracted and kept at +4ºC in 4% PFA solution overnight. To minimize PFA-induced autofluorescence, the brains were washed in cold phosphate buffered saline (PBS) for 3 days. Then the brains were immersed in 30% sucrose solution for 2-5 days and kept at -80°C until sectioning. Free floating 60 µm thick sagittal sections were obtained and mounted with 1/1 : glycerol/PBS solution.

Imaging of Synapses and Dendrites

High resolution, multispectral, 3D tile scans were obtained by a Zeiss LSM810 laser-scanning confocal microscope, using an oil objective (40×, NA: 1.3). x, y pixel and z-step sizes were determined for adequate acquisition of cyan eGRASP signal which has the lowest emission wavelength among other signals. Therefore, we adjusted the pixel size as 0.103 µm. Then, 30

µm-thick overlapping (10%) tile scans with field of view (FOV) of 205 × 205 µm^2 were obtained, spanning the full cortical thickness from surface to corpus callosum. For multispectral imaging, the same FOVs were imaged using 453, 488, 543 and 633 nm laser excitations. Emissions of fluorescent proteins were bandpass-filtered at 465-490 nm for cyan eGRASP under 453 nm excitation; 495-515, 515-535 and 535-555 nm for green and yellow eGRASP under 488 nm excitation; 550-630 nm for TagRFP-T under 543 nm excitation and 645-750 nm for autofluorescent signals under 633 nm excitation.

Confirmation of Multi-Colored eGRASP Signal Acquisition

To confirm expression of eGRASP proteins in mPFC pyramidal neurons, lambda scans were acquired via Zeiss LSM810 laser scanning confocal microscope. An area of ~105 × 105 µm^2 were scanned with 1024 × 1024 pixels using a 40× oil immersion objective (NA: 1.3). Excitation was performed with 453 and 488 nm lasers, to detect spectral emission profiles of cyan and green/yellow eGRASP, respectively. Fluorescence emission was collected in 5 nm-wide non-overlapping bands, between 460-575 nm for cyan and 495-600 nm for green/yellow eGRASP. A multispectral fluorescence data to be submitted to LUMoS for comparison was collected before the lambda scans at the same field of view, as described above. Lambda stacks were further processed with Stowers Spectral Unmixing plug-in of FIJI (61), to extract the emission spectra of specific eGRASP proteins.

Spectral lambda scans were used to validate LUMoS for unmixing cyan, green, yellow eGRASP signals from each other. In a region of interest with three different types of synaptic signals in the field, we first confirmed the presence of CFP, GFP and YFP, via checking their spectral emission profiles (Suppl. Fig. 2A-C) with reference spectra acquired from *fpbase.org* (62). Then, we processed the image data from the same field with LUMoS and unmixed with the same parameters as described above. We found ~100 % overlap (n = 4 stacks) between the LUMoS classification of CFP, YFP and GFP and with their ground-truth synapse distribution, respectively (Suppl. Fig. 2D-E).

Reflectance Imaging

Confocal reflectance imaging was performed to determine the boundary between layer VI and corpus callosum. Images were obtained in tile scans by a Leica SP8 confocal microscope. Briefly, a narrow band reflectance signal was obtained by excitation at 488 nm and emission at ~483-493 nm, using a RT15/85 beamsplitter. Z-stacks were obtained with 2-3 µm step size. The pixel size

for this setting was ~0.6 µm. Dendritic TagRFP-T labelled signals detected by 552 nm excitation were overlaid on the reflectance signal. Finally, images were stitched via stitching algorithm of LASX v3.5.5.19976.

Image Processing

Stitching: Acquired tiles were stitched together using the Zeiss Stitching algorithm (ZEN 3.2 Black Edition) or BigStitcher plug-in of FIJI (58). The correlation threshold was kept above "0" for Zeiss Stitching algorithm. For BigStitcher application, x1 downscaling was applied to prevent loss or duplication of signals in the overlapping regions.

Unmixing: Signals from dendrites and synapses overlapped in the acquired images. Unmixing both signals at the same time can cause interruptions to dendritic continuity, which will interfere with reconstruction. Therefore, we unmixed dendritic and synaptic signals separately by LUMoS plug-in of FIJI (31). Dendritic TagRFP-T signals were unmixed from the autofluorescent signals, whereas the synaptic yellow/green/cyan-eGRASP signals were unmixed from each other and auto-fluorescent signals (Fig.1-a,c). The unmixing process was repeated at least 50 times with 100 iterations. The reference image was selected from tile images and axial slices, where all signal subgroups (from all fluorophores as well as nonspecific autofluorescence) were observable within the field of view.

Deconvolution: To be able to generate a 3D reconstruction of the dendrites and synapses, deconvolution of the synaptic and dendritic signals was performed using GPU-based Richarson-Lucy algorithm (59). First, we prepared images by making the voxels isotropic via Reslice Z function in FIJI. Then point spread function (PSF) with the size of 256 x 256 x *N*, where *N* is the number of z-stacks of the tile image, was prepared by using Diffraction PSF 3D plug-in of FIJI. Optimum wavelengths of eGRASP proteins and TagRFP-T were used for PSF generation (28). Finally, Richardson-Lucy deconvolution algorithm with 20 iterations was applied for all signals. Synaptic signals were further processed by Gaussian filtering with a window size of 3 pixels. Stitched (BigStitcher) and unmixed (LUMoS) images were processed in Fiji.

Reconstruction: Synaptic and dendritic images were merged according to their tile locations. We reconstructed the dendrites using the automated approach in Gliko et al (2024) that combines U-Net convolutional neural network segmentation with post-processing to produce a digital reconstruction. The segmentation model that was trained with a set of brightfield images of mouse cortical excitatory neurons (32) was used without any tuning. Segmentation was post-

processed by thresholding the background, connected component analysis to remove short segments, skeletonization, and conversion to the .swc format, followed by pruning and down sampling. We did not determine the diameters of the dendritic branches. We also did not classify the dendrites into apical, basal, and oblique compartments since the directionality with respect to the soma could not be determined during imaging.

Definition of Dendritic Segments

Dendrites of all mPFC pyramidal neurons across all layers were labelled with TagRFP-T. Dendritic signals were intermingled and it was hard to decide if they belonged to the same dendritic tree or not, owing in part to the neuronal organization of mPFC and diffraction limit (0.25 - 0.35 µm) of confocal microscopy, and in part to the erroneous linkages between dendritic segments introduced by dendritic reconstruction. Therefore, we followed a conservative strategy and defined dendritic segments as part of the reconstructed tree between two adjacent branching or leaf nodes and evaluated the synapses only on these short dendritic segments. We excluded the segments resulting from image edge artefacts during quality control. Additional quality control was applied to remove (spurious) segments of 0 µm length.

Synapse Detection

BLA-mPFC, VH-mPFC and VTA-mPFC synapses were detected by the Synapse Detector plug-in of Vaa3D (33), which performs synapse detection via adaptive watershed segmentation within a given distance from the dendritic reconstruction. We ran this plug-in by the following five steps:

1- We thresholded deconvolved synaptic and segmented dendritic signals. Threshold values for synapses were determined by comparing raw synapse data and deconvolved synapse data (Fig. 2g, Suppl. Fig. 1). Threshold values for dendritic images were determined to avoid discontinuities along dendritic branches.

2- We prepared the 3D 8-bit RGB stacks that the Synapse Detector requires as input as follows:

$$I = [I_R, I_G, I_B] \tag{1}$$

$$I_R = I_{dendrite} \cup I_{synapse} \tag{2}$$

$$I_G = I_{synapse} \tag{3}$$

$$I_B = 0 \tag{4}$$

I_R, $I_G$and $I_B$indicate 8-bit images, sized H x W x Z (height x width x depth of the image stack). $I_{dendrite}$ indicates the segmented dendritic image stack, $I_{synapse}$ indicates the synapse image of size H x W x Z. I_R is the union of dendritic ($I_{dendrite}$) and synaptic image ($I_{synapse}$) stacks. I_B is a stack of all zeros since the the algorithm writes the detected synapse information on this third channel after detection.

3- Synapse Detector has 4 main parameters: minimum signal density threshold values for dendritic and synaptic images, minimum synapse volume and maximum search distance from .swc tree. We did not use the signal density threshold values for dendritic and synaptic images as we applied thresholding in step 1. We limited the analysis to those synapses detected within ≤ 20 pixels (~ 2 µm) distance around the swc tree(63) and those occupying at least 30 voxels (~ 0.030 μm^3) as the diffraction limit (0.25 - 0.35 µm) requires a detectable signal to occupy at least 3 pixels space (~ 0.3 µm) along each dimension.

4- The Graphical User Interface (GUI) of the Synapse Detector allows the user to examine the synapses segment-by-segment, include/exclude detected synapses from the analysis, adjust the detected synapse volumes, and annotate synaptic positions as dendrite-targeting or spine-targeting. While human-annotated synaptic mapping is the gold standard way of input mapping, such manual inspection is infeasible for large datasets. Therefore, we visually examined the automatically detected synapses using only a zoomed-out view within the GUI of Synapse Detector. If most of the synapses have been tagged as detected, we have extracted the outputs of the algorithm in .csv format.

5- We repeated the above 4 steps for each of the three different colored synapse separately.

The outputs of Synapse Detector Used in this study are:

- 3D spatial locations of detected synapses
- Volumes of the detected synapses
- For each synapse, the closest node on the dendritic segment from the detected synapse, which also includes dendritic segment and tree information.

Comparison Between Automatic and Manual Counting Results

We checked the accuracy of the Synapse Detector in automatic synapse detection by two means:

1- In randomly selected 3D stacks (n = 49 images with a size of ~600 x 2000 x 300 pixels from 15 cortical columns) from different layers, we confirmed each automatically detected synapse by visually inspecting and locating it in the unmixed images. Visual comparison was performed in Fiji by comparing detected synapses and the unmixed synaptic signals. Subsequently, the percentage of matched synapses among the total number of automatically detected synapses was calculated. This method suggests that 95.7% of automatically labeled synapses were truly synaptic signals and the percentage of true synapses was similar regardless of the brain region of origin of mPFC afferents (Suppl. Fig. 3A,B).

2- We manually counted all three types of synapses (formed by projections from BLA, VH and VTA) in randomly selected 3D frames from different layers on 3D visualization module of Vaa3D. Only signals within ~2 µm from the reconstruction tree were manually counted, as Synapse Detector was set to detect synapses within ~2 µm of a reconstructed dendrite. After manual labeling of synapses, spatial locations of the synapses were saved as a ".marker" file. We then computationally matched the spatial locations of manually detected synapses with automatically detected synapses using the Hungarian algorithm (64). Based on this, we initially found that 80.64 ± 11.74% of the manually annotated synapses were matched to automatically detected synapses, and 23.97 ± 12.13% of the automatically detected synapses were not annotated by the expert. Upon closer inspection, however, we found that the mismatches were overwhelmingly due to synapses with small volumes, making them more likely to be missed by the human (Suppl. Fig. 3C). We also observed that a majority of the unmatched manual annotations (~11,4% of all manually labeled synapses) were actually assigned to incorrect locations by the graphical user interface of Vaa3D, which infers the 3D location from a click on the 2D screen. After exclusion of these mislocated manual annotations from the calculation and inclusion of the smaller synapses, we found that the overall synapse detection performance was ~91%.

Definition of Cortical Layers and Preparation of Their Reconstructions

Boundaries between cortical layers were identified by using the parcellation scheme of Common Coordinate Framework of Allen Brain Atlas (65). Accordingly, layer I, II/III, V and VI have been expected to cover 8%, 14%, 61% and 17% of the cortical column, respectively. The mean ± standard deviation of the thickness for each layer were 113.83 ± 21.46 (Layer I), 194.72 ± 37.14 (Layer II/III), 858.31 ± 154.35 (Layer V) and 239.20 ± 43.02 (Layer VI). Layer V was then divided into 2 equal halves: layer Va and layer Vb. Then 3D cortical reconstructions were divided into laminae according to the identified vertical coordinates. Segments straddling two neighboring layers were excluded from the analysis.

Calculation of Percentages of Each Synapse-to-all Detected Synapses

After dividing cortical columns into cortical layers, we calculated the ratios of synapses made by each long-range projections originated from certain brain region (represented by color in the formula) to all detected synapses from all three brain regions. Let n_{layer}^{color} indicate number of synapses from BLA, VH or VTA in the layer I, II/III, Va, Vb or VI:

$$N_{layer} = n_{layer}^{cyan} + n_{layer}^{green} + n_{layer}^{yellow} \tag{5}$$

$$P_{layer}^{color} = \frac{n_{layer}^{color}}{N_{layer}} \times 100;\ color \in \{cyan, green, yellow\} \tag{6}$$

N_{layer} indicates numbers number of total detected synapses in a certain cortical layer. P_{layer}^{color} indicates the percentage of certain detected synapses color in given layer. We than created a color percentage matrix $M^{color}$for each color:

$$M_{i,layer}^{color} = P_{layer}^{color} \tag{7}$$

$M_{i,layer}^{color}$ indicates the percentage value of cyan, green or yellow eGRASP labeled synapses in certain $layer$ of cortical column i where i is the identity of cortical column. The expected size of the color percentage matrix is 5 x 13 (parts of cortical columns x number of mice) for each brain region projecting to mPFC.

Dimensionality Reduction Matrix for Principal Component Analysis

To apply dimension reduction first, M^{color} matrices belonging different brain regions were concatenated in 2 dimensions.

$$M^{P} = [M^{cyan}, M^{green}, M^{yellow}] \tag{8}$$

The final size of dimension reduction matrix (M^{P}) was 13 x 15. Then, principal component analysis was performed. The first and second principal components have been used for plotting low dimensional projection of percentages of "synapses made by single brain region-to-all detected synapses matrix.

Formation and Analysis of Closest Spatial Distance Matrix of BLA and VH Synapses

For BLA and VH synapses in layer Vb and layer VI, the first four closest spatial distances to BLA or VH synapses were measured. A 42,317 x 8 sized matrix was formed by appending closest VH and BLA synapse distances, respectively. Then Uniform Manifold Approximation and Projection (UMAP) was used to visualize synapses, behavioral profiles, social interaction scores, mouse IDs (34). Default values (version 0.5.5) were used for the hyperparameters of the UMAP code.

Random Forest Classifiers were formed using 10 forests with 75 trees. K-fold cross validation scheme with 10 independent parts was applied to each forest. In each fold, 10% of the dataset has been used as testing dataset. Only data labels have been randomized to train RF classifier to compare RF classification performance for structured and randomized datasets. Parametric measures of accuracy and F1 scores of RF classifier have been used for comparison between main data and randomly shuffled data. RF classifiers have been trained using sklearn v1.4.0 inside Python 3.9.

Statistical Analysis

Data are presented as median with interquartile ranges, mean ± S.E.M or mean with 95% confidence interval. Kruskal-Wallis (KW) test was used for multiple group comparisons and followed by pairwise comparisons by Mann Whitney U (MWU) tests, p values for MWU were adjusted by Bonferroni correction. All analysis were two tailed. p value less than 0.05 and 0.0167 were considered as significant in KW and post-hoc MWU tests, respectively. All statistical analysis was performed using Scipy v1.11.1. Plots were drawn by using Matplotlib v3.8.0 and Seaborn v0.12.2.

COMPETING INTERESTS

The authors declare that they have no competing interests.

AUTHOR CONTRIBUTIONS

STS, SEE and EEK were responsible for the design and conception of the study. STS, SEE and AC were responsible for the acquisition of data, STS, OG, SEE, AC, US and EEK were responsible for the analysis and interpretation of data. STS, US and EEK drafted the manuscript.

ACKNOWLEDGEMENTS

This study is supported by Research Fund of Hacettepe University, Grant number: TSA-2020-18753 to EEK. We thank Dr. Turgay Dalkara for his valuable opinions on the manuscript; Dr. Nevin Belder, Dr. Aslıhan Bahadır-Varol, Mesut Fırat and Anke Schönherr for their technical support. Graphical depictions inside Figure-1, Figure-2, Figure-6 and Graphical Abstract were prepared with Biorender.

MAIN FIGURE DESCRIPTIONS

Figure – 1: Description of the Experimental Strategy. a: AAV constructs used in the study. **b:** AAV injection sites, colored according to the e-GRASP constructs AAVs express. **c:** Schematic of a pyramidal mPFC neuron dendrite, tagged with TagRFP-T, that makes synapses with afferents from BLA, VH and VTA, each labelled with a different color. **d:** Timeline of the experimental procedure. **e:** Representative tracking images of SS (top) and SR (bottom) mice during the social interaction test. **f:** Social interaction scores. Data is shown as mean ± SEM. **g:** Tiled imaging scheme across an mPFC column covering all layers. **h:** Emission and excitation wavelengths used for multispectral confocal imaging. Emission wavelengths taken from *fpbase.org(62).*

Figure – 2: Image processing pipeline: Top: The schema of processing of tiled images. Bottom: Processing of individual tiles. Processing of the dendritic images is shown at the top, processing of the synaptic signals is shown at the bottom

Figure – 3: Labeling and detection of long-range inputs from VH, BLA and VTA to mPFC pyramidal neurons across the cortical column. Representative images from different steps of the image processing pipeline. **A:** raw image stack; **B:** unmixed image; **C:** deconvolved image; **D:** segmented image; **E:** top: dendritic reconstruction of the sample, bottom: image of the segmented stack overlaid on dendritic reconstruction; **F:** top: thresholded image stack, bottom: alpha blended version of the thresholded image; **G:** synapses detected by Synapse Detector (Vaa3D). **H:** deconvolved stack sample; **I-J:** zoomed in image of a sample dendritic segment inside the white dotted line box inside figure – 3H was shown. **I:** reconstruction of dendritic segment overlaid on the deconvolved image, **J:** ball and stick version of dendritic segment and its synapses Scale bar for figures 3A-G: 25 µm**;** scale bar for figure 3H: 20 µm; scale bar for figure 3I-J: 5 µm.

Figure – 4: Layer and stress phenotype-dependent changes of BLA, VH and VTA synapses. A-E: Percentage of BLA-to-all detected synapses in mPFC layers I-VI. **A:** Layer I (Kruskal-Wallis (KW) test: H = 4.02, p = 0.13); **B:** layer II/III (KW test: H = 5.53, p = 0.06); **C:** layer Va (KW test: H = 4.87, p = 0.08); **D:** layer Vb (KW test: H = 8.78, p = 0.012; Mann-Whitney U (MWU) test: p = 0.0158, SS vs SR ; p = 0.0158, SS vs SN ; p = 0.22, SR vs SN); **E:** layer VI (KW test: H = 10.50, p = 0.0052; MWU test: p = 0.0079, SS vs SR ; p = 0.0079, SS vs SN ; p = 0.15, SR vs SN). **F:** Correlation of layer Vb's BLA percentages with the SI ratio (Spearman correlation: rho = - 0.56, p = 0.030; linear regression: F(1,13) = 4.96, R^2 = 0.28, p = 0.044). **G:** Correlation of layer VI's BLA

percentages with the SI ratio (rho = - 0.75, p = 0.001, Spearman correlation; F(1,13) = 12.97, R^2 = 0.50, p = 0.003, Linear regression). **H:** Spearman correlations of BLA percentages in each layer with the social interaction (SI) ratio. Non-significant correlation coefficients and p-values were not shown. **I-M:** Percentage of VH-to-all detected synapses in mPFC layers I-VI. **I:** Layer I (KW test: H = 3.75, p = 0.15); **J:** layer II/III (KW test: H = 6.02, p = 0.049; MWU test: p = 0.54, SS vs SR ; p = 0.15, SS vs SN ; p = 0.0158, SR vs SN); **K:** layer Va (KW test: H = 7.57, p = 0.022; MWU test: p = 0.69, SS vs SR ; p = 0.0079, SS vs SN ; p = 0.055, SR vs SN, MWU test); **L:** layer Vb (KW test: H = 10.82, p = 0.0044; MWU test: p = 0.0079, SS vs SR ; p = 0.0079, SS vs SN ; p = 0.09, SR vs SN); **M:** layer VI (KW test: H = 9.50, p = 0.0086; MWU test: p = 0.0079, SS vs SR ; p = 0.0079, SS vs SN ; p = 0.69, SR vs SN). **N:** Correlation of layer Vb's VH percentages with the SI ratio (Spearman correlation: rho = 0.63, p = 0.012; Linear regression: F(1,13) = 8.33, R^2 = 0.39, p = 0.013). **O:** Correlation of layer VI's VH percentages with the SI ratio (Spearman correlation: rho = 0.69, p = 0.0040; Linear regression: F(1,13) = 9.80, R^2 = 0.43, p = 0.008). **P:** Spearman correlations of VH percentages in each layer with the SI ratio. Non-significant correlation coefficients and p-values were not shown. **Q-U:** Percentage of VTA-to-all detected synapses in mPFC layers I-VI. **Q:** Layer I (KW test: H = 0.11, p = 0.94); **R:** layer II/III (KW test: H = 2.47, p = 0.28); **S:** layer Va (KW test: H = 1.26, p = 0.53); **T:** layer Vb (KW test: H = 4.5, p = 0.10); **U:** layer VI (KW test: H = 4.34, p = 0.11). **V:** Correlation of layer Vb's VTA percentages with the SI ratio (Spearman correlation: rho = -0.34, p = 0.21; Linear regression: F(1,13) = 2.60, R^2 = 0.17, p = 0.13,). **W:** Correlation of layer VI's VTA percentages with the SI ratio (Spearman correlation: rho = - 0.16, p = 0.56; Linear regression: F(1,13) = 1.58, R^2 = 0.11, p = 0.23). **X:** Spearman correlations of VTA percentages in each layer with the social interaction (SI) ratio. Non-significant correlation coefficients and p-values were not shown. **Y:** Projection onto top 2 PCs of the synapse count data (synapse count per layer and afferent), for different behavioral groups. Data is presented as median and IQR for boxplots graphs. For layer I, n = 5 slices from 3 SN mice, n = 4 slices from 4 SR mice and n = 4 from 4 SS mice; for layers from II/III to VI, n = 5 from 3 SN mice, n = 5 from 4 SR mice and n = 5 from 3 SS mice. Asterisks in the figures stand for $**$: $p \leq 0.01$, and $*$: $p < 0.05$.

Figure – 5: The number of segments forming synapses with multiple brain regions increased in Layer VI of SS mice

A-E: Analysis of dendritic segments receiving inputs from a single brain region (monocolor) and from multiple brain regions (multicolor) in layer Vb. **A:** Pooled data from each group showing total numbers and percentages of dendritic segments receiving inputs from a single brain region

(monocolor) and from multiple brain regions (multicolor) in layer Vb. Number of monocolor segments in SN:SR:SS = 1,082:1,568:1,020. Number of multicolor segments in SN:SR:SS = 604:1,317:1,237. **B:** Percentage of dendritic segments receiving input from at least 2 different brain regions in layer Vb (Kruskal-Wallis (KW) test: H = 2.96, p = 0.22). **C:** Correlation of the ratio of multicolor dendritic segments in layer Vb with the SI ratio. (Spearman correlation: rho = - 0.18, p = 0.49; linear regression: F(1,13) = 0.02, R^2 = 0.0016, p = 0.88). **D:** Pooled data from each group showing total number and percentages of dendritic segments receiving input from multiple brain areas in layer Vb. **E:** Comparisons of percentages of dendritic segments receiving input from VTA & BLA (KW test: H = 12.58, p = 0.0018; Mann Whitney-U (MWU) test: p= 0.0079, SS vs SR; p = 0.011, SS vs SN; p = 0.011, SR vs SN), VTA & VH (KW test: H = 3.88, p = 0.14), VH & BLA (KW test: H = 1.93, p = 0.37) and VTA & VH & BLA (KW test: H = 3.31, p = 0.19). **F-J:** Same as a-e for layer VI. **F:** For layer VI, number of monocolor segments in SN:SR:SS = 352:1,589:465, number of multicolor segments in SN:SR:SS = 197:628:1,015. **G:** Percentage of dendritic segments receiving input from at least 2 different brain regions in layer VI (KW test: H = 8.66, p = 0.013; MWU test: p = 0.015, SS vs SR; p = 0.0079, SS vs SN; p = 0.84, SN vs SS). **H:** Correlation of multicolor dendritic segments in layer VI with SI ratio (Spearman correlation : rho = - 0.63, p = 0.010; linear regression: F(1,13) = 7.31, R^2 = 0.36, p = 0.018). **I:** Same as d for layer VI. **J:** Comparisons of percentages of dendritic segments receiving input: VTA & BLA (KW test: H = 2.61, p = 0.27); VTA & VH (KW test: H = 9.08, p = 0.010; MWU test: p = 0.11, SS vs SR ; p = 0.0079, SS vs SN ; p = 0.055, SR vs SN); VH & BLA (KW test: H = 3.46, p = 0.17); VTA & VH & BLA (KW test: H = 3.31, p = 0.19). Data shown as median and IQR. Asterisks in the figures stand for $**$: $p \leq 0.01$, and $*$: $p < 0.05$. For both layers, n = 5 from 3 SN mice, n = 5 from 4 SR mice and n = 5 from 3 SS mice.

Figure – 6: Euclidean Distances Between Unidentical, but not Identical Synapses were Distinct in SS mice

A: Histograms of distances between each VH synapses and its closest VH synapse for different groups. **B:** Histograms of distances between each BLA synapse and its closest BLA synapse for different groups. **C:** Histograms of distances between each VH synapse and its closest BLA synapse for different groups. **D:** Histograms of distances between each BLA synapse and its closest VH synapse for different groups. **E-F:** Cartoon illustration of spatial organization of BLA and VH synapses in layer Vb and VI of **E.** SN/SR and **F.** SS mice. **G:** Comparison of accuracy after Random Forest Classification between observed and randomized data ($p = 5.16 \times 10^{-5}$, independent samples t-test). **H:** Confusion matrices of observed data (left) and randomized data

(right). Values were normalized for the number of true labels. **J:** F1 scores for behavioral groups. For SN mice: $p = 1.83 \times 10^{-24}$; for SR mice: $p = 2.34 \times 10^{-23}$; for SS mice: $p = 2.12 \times 10^{-30}$, independent samples t-test. **K-L:** 2D UMAP projection of Euclidean distances to four closest VH and four closest BLA synapses. **l:** colored by behavioral groups, **m:** colored by SI Ratio. Data is presented as mean and 95% CI. ***: $p < 0.001$; **: $p < 0.01$; *: $p < 0.05$. n = 5 from 3 SN mice, n = 5 from 4 SR mice and n = 5 from 3 SS mice.

Supplemental Table 1. Characteristics of the Adeno-associated-virus, their injection areas and volumes

Virus	Density (vg/μL)	Volume (μL)	Area
AAV2/1-CaMKIIα-yellow pre-eGRASP (p32)	6.67×10^9	1	BLA
AAV2/1-CaMKIIα-green pre-eGRASP (p32)	6.65×10^9	1	VH
AAV2/1-CaMKIIα- cyan pre-eGRASP (p30)	6.8×10^9	1	VTA
AAV2/1-DIO-TagRFP-T -p2A-post-eGRASP	6.79×10^8	0.25	mPFC
AAV2/1-CaMKIIα-iCre	4×10^8	0.25	mPFC

SUPPLEMENTAL FIGURE DESCRIPTIONS

Supplemental Figure – 1: Sample Image Processing for Each Signal

A: Sample image processing for dendritic signals. **B:** Sample image processing for synaptic signals from top to bottom: VTA (cyan eGRASP), VH (green eGRASP) and BLA (yellow eGRASP). Scale bar: 25 µm

Supplemental Figure – 2: Validation of LUMoS spectral unmixing

A: Normalized intensity spectrums generated from lambda scans of eGRASP proteins overlaid with reference eCFP, eGFP and TagYFP spectral emission curves obtained from *fpbase.org (62).* The peaks of emission wavelengths of eGRASP proteins aligned well with those of eCFP, eGFP and TagYFP, respectively. **B:** Linear unmixing of cyan and green eGRASP signals, under 458 nm excitation and spectral profiling between 460-575 nm emission range. Note that 458 nm can excite both cyan and green eGRASP proteins. Cyan eGRASP has left-shifted emission peak compared to green eGRASP, allowing separation of signals via linear unmixing. **i:** zoomed-in image of cyan eGRASP, **ii:** zoomed-in image of green eGRASP and **iii:** zoomed-in image of yellow eGRASP which is not visible due to ineffective excitation of yellow eGRASP with 458 nm laser. **C:** Linear unmixing of green and yellow eGRASP signals, under 488 nm excitation and spectral profiling between 495-600 nm emission range. 488 nm can excite both green and yellow eGRASP. Green eGRASP has left-shifted emission peak compared to yellow eGRASP, allowing separation of signals via linear unmixing. **i:** zoomed-in image of cyan eGRASP which is not visible due to ineffective excitation of cyan eGRASP with 488 nm laser, **ii:** zoomed-in image of green eGRASP and **iii:** zoomed-in image of yellow eGRASP. **D:** Image field containing cyan, green and yellow eGRASP proteins, shown as a composite image with different emission bands shown in different colors. The pixels corresponding to the 495-515 and 515-535 nm emission windows were pseudocolored as red and green respectively. **i:** zoomed-in image of cyan eGRASP signals were shown as cyan-colored signals. **ii:** Green eGRASP signals are visible as yellow-colored signals, as a result of mixing of green and red signals. At this setting, the emission intensity of green eGRASP proteins would be higher in the 495-515 nm window (**a**) than 515-535 nm window (**b**). Therefore, the pseudocolor of the signal would shift towards red (hence yellow). **iii:** Yellow eGRASP are visible as green-colored signals. At this setting, the emission intensity of yellow eGRASP proteins would be higher in the 515-535 nm window (**b**) than 495-515 nm window (**a**). Therefore, the pseudocolor of the signal would shift towards green. **E:** Output of LUMoS spectral

unmixing of the same image field with cyan, green and yellow eGRASP proteins were shown as their corresponding colors. **i:** zoomed-in image of cyan eGRASP signals, **ii:** zoomed-in image of green eGRASP and **iii:** zoomed-in image of yellow eGRASP. Note that all LUMoS classification of synapses is in line with their spectral profile confirmation as eCFP, tagYFP or eGFP.

Supplemental Figure – 3: Accuracy of synapse detection for different synapse types and behavior phenotypes

A: Percentage of visually confirmed unmixed synapses among automatically detected synapses distributed for different brain regions (p = 0.12, Kruskal-Wallis test). **B:** Percentages of the automatically detected synapses that are confirmed by an expert. **C:** Comparison of mean synaptic volumes of spatially matched and unmatched synapses which were detected automatically. (p = 2.57 x 10-8, Mann-Whitney U test). Spatially unmatched synapses had lower mean synapse volume than spatially matched synapses. Data is presented as mean and 95% CI in Figure A and B; as median withing interquartile range in Figure C.

Supplemental Figure – 4: Chronic stress increased and decreased the percentages of BLA--to-all detected synapses and VH-to-all detected synapses, respectively in superficial layers of mPFC.

A: Representative unmixed image of a cortical column covering all layers of mPFC. Scale bar: 200 µm. **B:** Pooled data from each group showing percentages of BLA, VH and VTA synapses. **C:** Comparison of percentages of BLA-to-all detected synapses in mPFC layers I and II/III between stressed and stress naïve groups. Left: Layer I, p = 0.06; right: Layer II/III, p = 0.019, Mann-Whitney U test. **D:** Comparison of percentages of VH-to-all detected synapses in mPFC layers I and II/III between stressed and stress naïve groups. Left: Layer I, p = 0.17; right: Layer II/III, p = 0.019, Mann-Whitney U test. **E:** Comparison of percentages of VTA-to-all detected synapses in mPFC layers I and II/III between stressed and stress naïve groups. Left: Layer I, p = 0.83; right: Layer II/III, p = 0.85, Mann-Whitney U test. Data shown as median and IQR.

Supplemental Figure – 5: The number of dendritic segments forming synapses with afferents from a single brain region in Layer Vb and VI.

A: Pooled data from each group showing total number and percentages of dendritic segments forming at least two synapses with afferents from only one brain region (yellow colored for BLA-only, green colored for VH-only and cyan colored for VTA-only) and from multiple brain regions

(purple colored) in layer Vb. **B:** Percentages of BLA-only-to-all segments with at least 2 synapses in layer Vb. Kruskal – Wallis (KW) Test: H= 7.79, p = 0.020; Mann-Whitney U (MWU) test: SS vs SR , p = 0.055; SS vs SN , p = 0.021; SR vs SN , p = 0.20. **C:** Percentages of VH-only-to-all segments with at least 2 synapses in layer Vb. KW test: H = 9.62, p = 0.0081; MWU test: SS vs SR , p = 0.0079; SS vs SN , p = 0.0079; SR vs SN , p = 0.54. **D:** Percentages of VTA-only-to-all segments with at least 2 synapses in layer Vb. KW test: H = 0.96, p = 0.61. **E:** Correlation of the percentage of BLA-only-to-all segments with at least 2 synapses with the SI ratio in layer Vb. (Spearman correlation: rho = - 0.55, p = 0.029; Linear regression: F(1,13) = 3.23, R^2 = 0.20, p = 0.09). **F:** Correlation of the percentage of VH-only-to-all segments with at least 2 synapses with the SI ratio in layer Vb. (Spearman correlation: rho = 0.57, p = 0.025; Linear regression: F(1,13) = 2.75, R^2 = 0.17, p = 0.12). **G:** Correlation of the percentage of VTA-only-to-all segments with at least 2 synapses with the SI ratio in layer Vb. (Spearman correlation: rho = - 0.15, p = 0.57; Linear regression: F(1,13) = 1.89, R^2 = 0.13, p = 0.19). **H:** Pooled data from each group showing total number and percentages of dendritic segments forming at least two synapses with afferents from only one brain region (yellow colored for BLA-only, green colored for VH-only and cyan colored for VTA-only) and from multiple brain regions (purple colored) in layer VI. **I:** Percentages of BLA-only-to-all segments with at least 2 synapses in layer VI. (KW test: H = 5.82, p = 0.054). **J:** Percentages of VH-only-to-all segments with at least 2 synapses in layer VI. (KW test: H = 9.42, p = 0.0090; MWU test: SS vs SR, p = 0.0079; SS vs SN , p = 0.0079; SR vs SN , p = 0.84). **K:** Percentages of VTA-only-to-all segments with at least 2 synapses in layer VI. (KW test: H = 0.28, p = 0.86). **L:** Correlation of the percentage of BLA-only-to-all segments with at least 2 synapses with the SI ratio in layer VI. (Spearman correlation: rho = - 0.61, p = 0.013; Linear regression: F(1,13) = 3.92, R^2 = 0.23, p = 0.06). **M:** Correlation of the percentage of VH-only-to-all segments with at least 2 synapses with the SI ratio in layer VI. (Spearman correlation: rho = 0.63, p = 0.010; Linear regression: F(1,13) = 9.32, R^2 = 0.42, p = 0.0092). **N:** Correlation of the percentage of VTA-only-to-all segments with at least 2 synapses with the SI ratio in layer VI. (Spearman correlation: rho = - 0.02, p = 0.94; Linear regression: F(1,13) = 0.16, R^2 = 0.01, p = 0.69)

SUPPLEMENTAL VIDEO DESCRIPTIONS

Supplemental Video – 1: Synapses aligned with dendritic reconstruction.

Supplemental Video – 2: Dendritic reconstruction and BLA, VH and VTA synapses throughout mPFC laminae.

REFERENCES

1. **Cook SC, and Wellman CL**. Chronic stress alters dendritic morphology in rat medial prefrontal cortex. *J Neurobiol* 60: 236-248, 2004.

2. **Liston C, Miller MM, Goldwater DS, Radley JJ, Rocher AB, Hof PR, Morrison JH, and McEwen BS**. Stress-induced alterations in prefrontal cortical dendritic morphology predict selective impairments in perceptual attentional set-shifting. *J Neurosci* 26: 7870-7874, 2006.

3. **Radley JJ, Arias CM, and Sawchenko PE**. Regional differentiation of the medial prefrontal cortex in regulating adaptive responses to acute emotional stress. *J Neurosci* 26: 12967-12976, 2006.

4. **Goldwater DS, Pavlides C, Hunter RG, Bloss EB, Hof PR, McEwen BS, and Morrison JH**. Structural and functional alterations to rat medial prefrontal cortex following chronic restraint stress and recovery. *Neuroscience* 164: 798-808, 2009.

5. **Hercher C, Canetti L, Turecki G, and Mechawar N**. Anterior cingulate pyramidal neurons display altered dendritic branching in depressed suicides. *J Psychiatr Res* 44: 286-293, 2010.

6. **Moda-Sava RN, Murdock MH, Parekh PK, Fetcho RN, Huang BS, Huynh TN, Witztum J, Shaver DC, Rosenthal DL, Alway EJ, Lopez K, Meng Y, Nellissen L, Grosenick L, Milner TA, Deisseroth K, Bito H, Kasai H, and Liston C**. Sustained rescue of prefrontal circuit dysfunction by antidepressant-induced spine formation. *Science* 364: 2019.

7. **Shansky RM, Hamo C, Hof PR, McEwen BS, and Morrison JH**. Stress-induced dendritic remodeling in the prefrontal cortex is circuit specific. *Cereb Cortex* 19: 2479-2484, 2009.

8. **Anastasiades PG, and Carter AG**. Circuit organization of the rodent medial prefrontal cortex. *Trends Neurosci* 44: 550-563, 2021.

9. **Fillinger C, Yalcin I, Barrot M, and Veinante P**. Afferents to anterior cingulate areas 24a and 24b and midcingulate areas 24a' and 24b' in the mouse. *Brain Struct Funct* 222: 1509-1532, 2017.

10. **Covington HE, 3rd, Lobo MK, Maze I, Vialou V, Hyman JM, Zaman S, LaPlant Q, Mouzon E, Ghose S, Tamminga CA, Neve RL, Deisseroth K, and Nestler EJ**. Antidepressant effect of optogenetic stimulation of the medial prefrontal cortex. *J Neurosci* 30: 16082-16090, 2010.

11. **Chaudhury D, Walsh JJ, Friedman AK, Juarez B, Ku SM, Koo JW, Ferguson D, Tsai HC, Pomeranz L, Christoffel DJ, Nectow AR, Ekstrand M, Domingos A, Mazei-Robison MS, Mouzon E, Lobo MK, Neve RL, Friedman JM, Russo SJ, Deisseroth K, Nestler EJ, and Han MH**. Rapid regulation of depression-related behaviours by control of midbrain dopamine neurons. *Nature* 493: 532-536, 2013.

12. **Friedman AK, Walsh JJ, Juarez B, Ku SM, Chaudhury D, Wang J, Li X, Dietz DM, Pan N, Vialou VF, Neve RL, Yue Z, and Han MH**. Enhancing depression mechanisms in midbrain dopamine neurons achieves homeostatic resilience. *Science* 344: 313-319, 2014.

13. **Carreno FR, Donegan JJ, Boley AM, Shah A, DeGuzman M, Frazer A, and Lodge DJ**. Activation of a ventral hippocampus-medial prefrontal cortex pathway is both necessary and sufficient for an antidepressant response to ketamine. *Mol Psychiatry* 21: 1298-1308, 2016.

14. **Felix-Ortiz AC, Burgos-Robles A, Bhagat ND, Leppla CA, and Tye KM**. Bidirectional modulation of anxiety-related and social behaviors by amygdala projections to the medial prefrontal cortex. *Neuroscience* 321: 197-209, 2016.

15. **Burgos-Robles A, Kimchi EY, Izadmehr EM, Porzenheim MJ, Ramos-Guasp WA, Nieh EH, Felix-Ortiz AC, Namburi P, Leppla CA, Presbrey KN, Anandalingam KK, Pagan-Rivera PA, Anahtar M, Beyeler A, and Tye KM**. Amygdala inputs to prefrontal cortex guide behavior amid conflicting cues of reward and punishment. *Nat Neurosci* 20: 824-835, 2017.

16. **Klavir O, Prigge M, Sarel A, Paz R, and Yizhar O**. Manipulating fear associations via optogenetic modulation of amygdala inputs to prefrontal cortex. *Nat Neurosci* 20: 836-844, 2017.

17. **Sotres-Bayon F, Sierra-Mercado D, Pardilla-Delgado E, and Quirk GJ**. Gating of fear in prelimbic cortex by hippocampal and amygdala inputs. *Neuron* 76: 804-812, 2012.

18. **Adhikari A, Topiwala MA, and Gordon JA**. Synchronized activity between the ventral hippocampus and the medial prefrontal cortex during anxiety. *Neuron* 65: 257-269, 2010.

19. **Adhikari A, Topiwala MA, and Gordon JA**. Single units in the medial prefrontal cortex with anxiety-related firing patterns are preferentially influenced by ventral hippocampal activity. *Neuron* 71: 898-910, 2011.

20. **Woo E, Sansing LH, Arnsten AFT, and Datta D**. Chronic Stress Weakens Connectivity in the Prefrontal Cortex: Architectural and Molecular Changes. *Chronic Stress (Thousand Oaks)* 5: 24705470211029254, 2021.

21. **Little JP, and Carter AG**. Subcellular synaptic connectivity of layer 2 pyramidal neurons in the medial prefrontal cortex. *J Neurosci* 32: 12808-12819, 2012.

22. **Little JP, and Carter AG**. Synaptic mechanisms underlying strong reciprocal connectivity between the medial prefrontal cortex and basolateral amygdala. *J Neurosci* 33: 15333-15342, 2013.

23. **Liu X, and Carter AG**. Ventral Hippocampal Inputs Preferentially Drive Corticocortical Neurons in the Infralimbic Prefrontal Cortex. *J Neurosci* 38: 7351-7363, 2018.

24. **Herry C, Ciocchi S, Senn V, Demmou L, Muller C, and Luthi A**. Switching on and off fear by distinct neuronal circuits. *Nature* 454: 600-606, 2008.

25. **Sanchez-Bellot C, AlSubaie R, Mishchanchuk K, Wee RWS, and MacAskill AF**. Two opposing hippocampus to prefrontal cortex pathways for the control of approach and avoidance behaviour. *Nat Commun* 13: 339, 2022.

26. **Choi JH, Sim SE, Kim JI, Choi DI, Oh J, Ye S, Lee J, Kim T, Ko HG, Lim CS, and Kaang BK**. Interregional synaptic maps among engram cells underlie memory formation. *Science* 360: 430-435, 2018.

27. **Connor SA, and Siddiqui TJ**. Synapse organizers as molecular codes for synaptic plasticity. *Trends Neurosci* 46: 971-985, 2023.

28. **Choi DI, and Kaang BK**. Interrogating structural plasticity among synaptic engrams. *Curr Opin Neurobiol* 75: 102552, 2022.

29. **Sudhof TC**. Neuroligins and neurexins link synaptic function to cognitive disease. *Nature* 455: 903-911, 2008.

30. **Golden SA, Covington HE, 3rd, Berton O, and Russo SJ**. A standardized protocol for repeated social defeat stress in mice. *Nat Protoc* 6: 1183-1191, 2011.

31. **McRae TD, Oleksyn D, Miller J, and Gao YR**. Robust blind spectral unmixing for fluorescence microscopy using unsupervised learning. *PLoS One* 14: e0225410, 2019.

32. **Gliko O, Mallory M, Dalley R, Gala R, Gornet J, Zeng H, Sorensen S, and Sümbül U**. High-throughput analysis of dendritic and axonal arbors reveals transcriptomic correlates of neuroanatomy. *bioRxiv* 2022.2003.2007.482900, 2024.

33. **Iascone DM, Li Y, Sumbul U, Doron M, Chen H, Andreu V, Goudy F, Blockus H, Abbott LF, Segev I, Peng H, and Polleux F**. Whole-Neuron Synaptic Mapping Reveals Spatially Precise Excitatory/Inhibitory Balance Limiting Dendritic and Somatic Spiking. *Neuron* 106: 566-578 e568, 2020.

34. **McInnes L, Healy J, and Melville J**. Umap: Uniform manifold approximation and projection for dimension reduction. *arXiv preprint arXiv:180203426* 2018.

35. **Sesack SR, Deutch AY, Roth RH, and Bunney BS**. Topographical organization of the efferent projections of the medial prefrontal cortex in the rat: an anterograde tract-tracing study with Phaseolus vulgaris leucoagglutinin. *J Comp Neurol* 290: 213-242, 1989.

36. **McGarry LM, and Carter AG**. Prefrontal Cortex Drives Distinct Projection Neurons in the Basolateral Amygdala. *Cell Rep* 21: 1426-1433, 2017.

37. **Tanimizu T, Kenney JW, Okano E, Kadoma K, Frankland PW, and Kida S**. Functional Connectivity of Multiple Brain Regions Required for the Consolidation of Social Recognition Memory. *J Neurosci* 37: 4103-4116, 2017.

38. **Hitti FL, and Siegelbaum SA**. The hippocampal CA2 region is essential for social memory. *Nature* 508: 88-92, 2014.

39. **Okuyama T, Kitamura T, Roy DS, Itohara S, and Tonegawa S**. Ventral CA1 neurons store social memory. *Science* 353: 1536-1541, 2016.

40. **Lee E, Rhim I, Lee JW, Ghim JW, Lee S, Kim E, and Jung MW**. Enhanced Neuronal Activity in the Medial Prefrontal Cortex during Social Approach Behavior. *J Neurosci* 36: 6926-6936, 2016.

41. **Likhtik E, Stujenske JM, Topiwala MA, Harris AZ, and Gordon JA**. Prefrontal entrainment of amygdala activity signals safety in learned fear and innate anxiety. *Nat Neurosci* 17: 106-113, 2014.

42. **Silverstein SE, O'Sullivan R, Bukalo O, Pati D, Schaffer JA, Limoges A, Zsembik L, Yoshida T, O'Malley JJ, Paletzki RF, Lieberman AG, Nonaka M, Deisseroth K, Gerfen CR, Penzo MA, Kash TL, and Holmes A**. A distinct cortical code for socially learned threat. *Nature* 626: 1066-1072, 2024.

43. **Padilla-Coreano N, Canetta S, Mikofsky RM, Alway E, Passecker J, Myroshnychenko MV, Garcia-Garcia AL, Warren R, Teboul E, Blackman DR, Morton MP, Hupalo S, Tye KM, Kellendonk C, Kupferschmidt DA, and Gordon JA**. Hippocampal-Prefrontal Theta Transmission Regulates Avoidance Behavior. *Neuron* 104: 601-610 e604, 2019.

44. **Kaidanovich-Beilin O, Lipina T, Vukobradovic I, Roder J, and Woodgett JR**. Assessment of social interaction behaviors. *J Vis Exp* 2011.

45. **Lissek S, Rabin S, Heller RE, Lukenbaugh D, Geraci M, Pine DS, and Grillon C**. Overgeneralization of conditioned fear as a pathogenic marker of panic disorder. *Am J Psychiatry* 167: 47-55, 2010.

46. **Jovanovic T, Kazama A, Bachevalier J, and Davis M**. Impaired safety signal learning may be a biomarker of PTSD. *Neuropharmacology* 62: 695-704, 2012.

47. **Lissek S, Kaczkurkin AN, Rabin S, Geraci M, Pine DS, and Grillon C**. Generalized anxiety disorder is associated with overgeneralization of classically conditioned fear. *Biol Psychiatry* 75: 909-915, 2014.

48. **Kaczkurkin AN, Burton PC, Chazin SM, Manbeck AB, Espensen-Sturges T, Cooper SE, Sponheim SR, and Lissek S**. Neural Substrates of Overgeneralized Conditioned Fear in PTSD. *Am J Psychiatry* 174: 125-134, 2017.

49. **Fetcho RN, Hall BS, Estrin DJ, Walsh AP, Schuette PJ, Kaminsky J, Singh A, Roshgodal J, Bavley CC, Nadkarni V, Antigua S, Huynh TN, Grosenick L, Carthy C, Komer L, Adhikari A, Lee FS, Rajadhyaksha AM, and Liston C**. Regulation of social interaction in mice by a frontostriatal circuit modulated by established hierarchical relationships. *Nat Commun* 14: 2487, 2023.

50. **Yizhar O, Fenno LE, Prigge M, Schneider F, Davidson TJ, O'Shea DJ, Sohal VS, Goshen I, Finkelstein J, Paz JT, Stehfest K, Fudim R, Ramakrishnan C, Huguenard JR, Hegemann P, and Deisseroth K**. Neocortical excitation/inhibition balance in information processing and social dysfunction. *Nature* 477: 171-178, 2011.

51. **Sun Q, Li X, Ren M, Zhao M, Zhong Q, Ren Y, Luo P, Ni H, Zhang X, Zhang C, Yuan J, Li A, Luo M, Gong H, and Luo Q**. A whole-brain map of long-range inputs to GABAergic interneurons in the mouse medial prefrontal cortex. *Nat Neurosci* 22: 1357-1370, 2019.

52. **Lee AT, Cunniff MM, See JZ, Wilke SA, Luongo FJ, Ellwood IT, Ponnavolu S, and Sohal VS**. VIP Interneurons Contribute to Avoidance Behavior by Regulating Information Flow across Hippocampal-Prefrontal Networks. *Neuron* 102: 1223-1234 e1224, 2019.

53. **Soumier A, and Sibille E**. Opposing effects of acute versus chronic blockade of frontal cortex somatostatin-positive inhibitory neurons on behavioral emotionality in mice. *Neuropsychopharmacology* 39: 2252-2262, 2014.

54. **Perova Z, Delevich K, and Li B**. Depression of excitatory synapses onto parvalbumin interneurons in the medial prefrontal cortex in susceptibility to stress. *J Neurosci* 35: 3201-3206, 2015.

55. **Harris AZ, Atsak P, Bretton ZH, Holt ES, Alam R, Morton MP, Abbas AI, Leonardo ED, Bolkan SS, Hen R, and Gordon JA**. A Novel Method for Chronic Social Defeat Stress in Female Mice. *Neuropsychopharmacology* 43: 1276-1283, 2018.

56. **Schindelin J, Arganda-Carreras I, Frise E, Kaynig V, Longair M, Pietzsch T, Preibisch S, Rueden C, Saalfeld S, Schmid B, Tinevez JY, White DJ, Hartenstein V, Eliceiri K, Tomancak P, and Cardona A**. Fiji: an open-source platform for biological-image analysis. *Nat Methods* 9: 676-682, 2012.

57. **Peng H, Bria A, Zhou Z, Iannello G, and Long F**. Extensible visualization and analysis for multidimensional images using Vaa3D. *Nat Protoc* 9: 193-208, 2014.

58. **Horl D, Rojas Rusak F, Preusser F, Tillberg P, Randel N, Chhetri RK, Cardona A, Keller PJ, Harz H, Leonhardt H, Treier M, and Preibisch S**. BigStitcher: reconstructing high-resolution image datasets of cleared and expanded samples. *Nat Methods* 16: 870-874, 2019.

59. **Perdigão LMA, Yee NBy, Ho EML, Pennington AH, King ONF, Darrow MC, and Basham M**. Computing for Optimized Biological Microscopy Data Processing and Analysis at The Rosalind Franklin Institute. *Microscopy and Microanalysis* 28: 1462-1464, 2022.

60. **Kim J, Zhao T, Petralia RS, Yu Y, Peng H, Myers E, and Magee JC**. mGRASP enables mapping mammalian synaptic connectivity with light microscopy. *Nat Methods* 9: 96-102, 2011.

61. **Unruh J**. Stowers ImageJ Plugins: https://github.com/jayunruh/Jay_Plugins.

62. **Lambert TJ**. FPbase: a community-editable fluorescent protein database. *Nat Methods* 16: 277-278, 2019.

63. **Shao LX, Liao C, Gregg I, Davoudian PA, Savalia NK, Delagarza K, and Kwan AC**. Psilocybin induces rapid and persistent growth of dendritic spines in frontal cortex in vivo. *Neuron* 109: 2535-2544 e2534, 2021.

64. **Kuhn HW**. The Hungarian method for the assignment problem. *Naval Research Logistics Quarterly* 2: 83-97, 1955.

65. **Wang Q, Ding SL, Li Y, Royall J, Feng D, Lesnar P, Graddis N, Naeemi M, Facer B, Ho A, Dolbeare T, Blanchard B, Dee N, Wakeman W, Hirokawa KE, Szafer A, Sunkin SM, Oh SW, Bernard A, Phillips JW, Hawrylycz M, Koch C, Zeng H, Harris JA, and Ng L**. The Allen Mouse Brain Common Coordinate Framework: A 3D Reference Atlas. *Cell* 181: 936-953 e920, 2020.

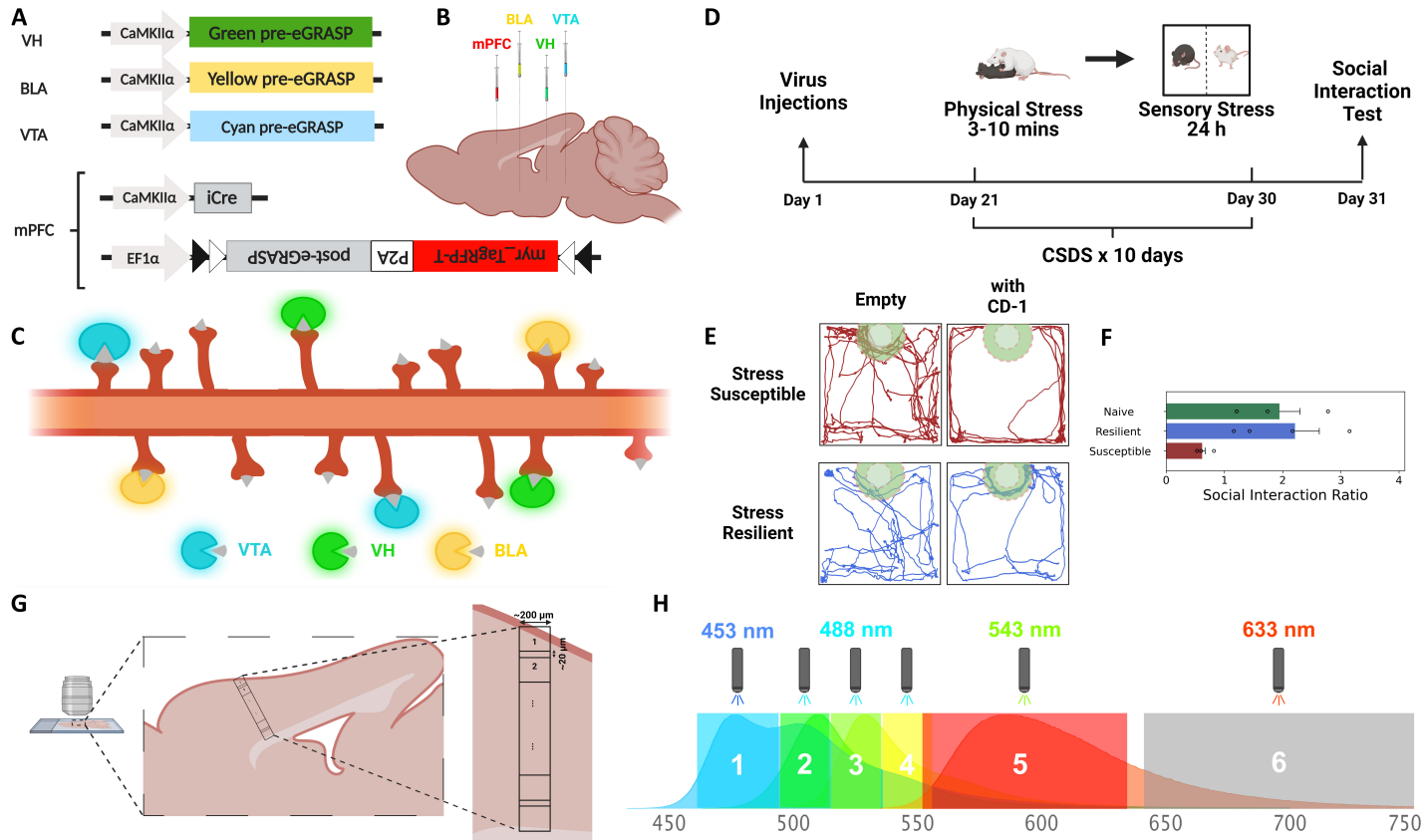
A
VH
BLA
VTA
mPFC
CaMKIIα
Green pre-eGRASP
Yellow pre-eGRASP
Cyan pre-eGRASP
iCre
EF1α
post-eGRASP
P2A
myr_TagRFP-T
B
BLA
VTA
mPFC
VH
C
VTA
VH
BLA
D
Virus Injections
Physical Stress 3-10 mins
Sensory Stress 24 h
Social Interaction Test
Day 1
Day 21
Day 30
Day 31
CSDS x 10 days
E
Empty
with CD-1
Stress Susceptible
Stress Resilient
F
Naive
Resilient
Susceptible
0
1
2
3
4
Social Interaction Ratio
G
~200 µm
~20 µm
1
2
H
453 nm
488 nm
543 nm
633 nm
1
2
3
4
5
6
450
500
550
600
650
700
750

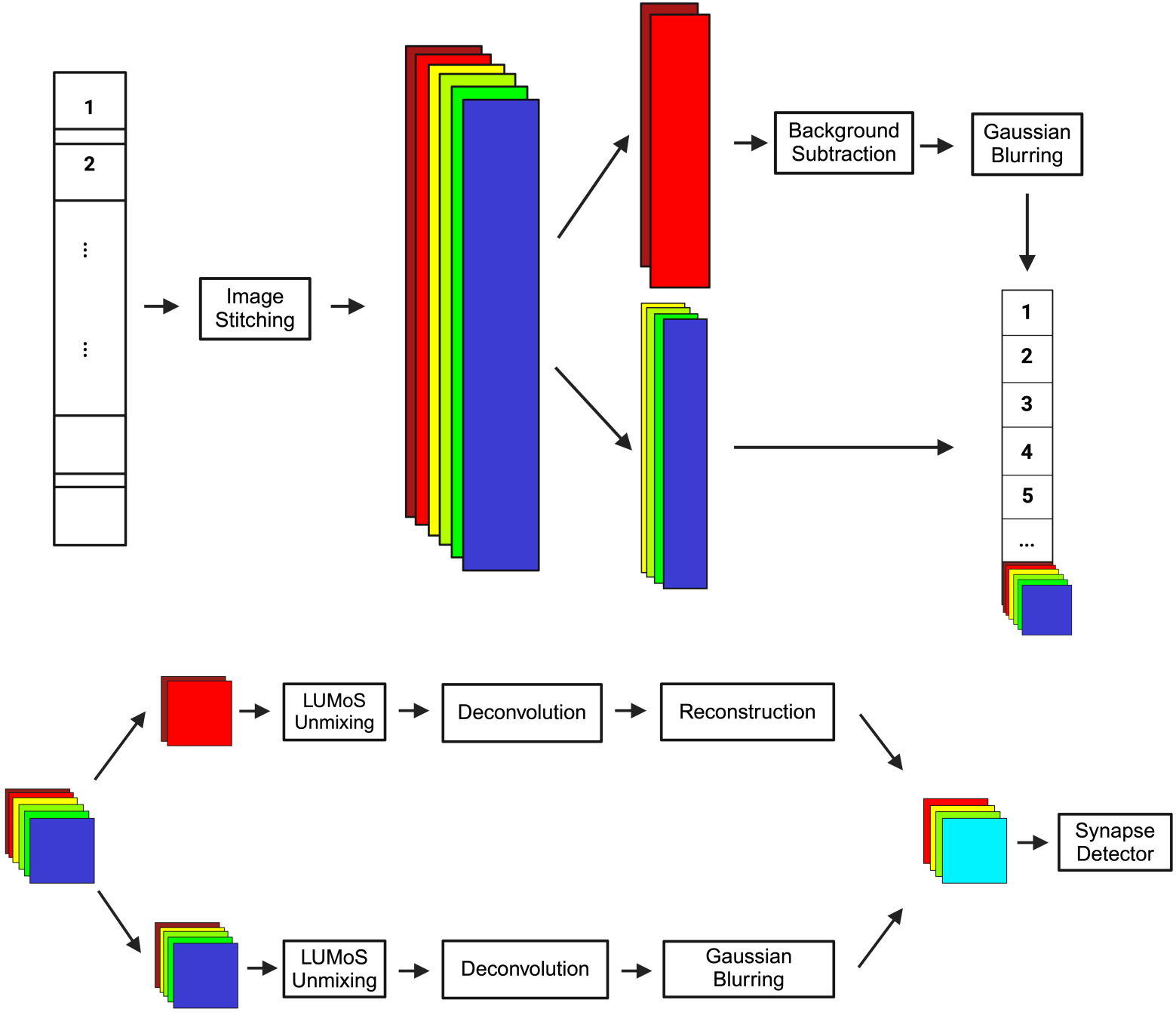
1
2
Image Stitching
Background Subtraction
Gaussian Blurring
1
2
3
4
5
...
LUMoS Unmixing
Deconvolution
Reconstruction
LUMoS Unmixing
Deconvolution
Gaussian Blurring
Synapse Detector

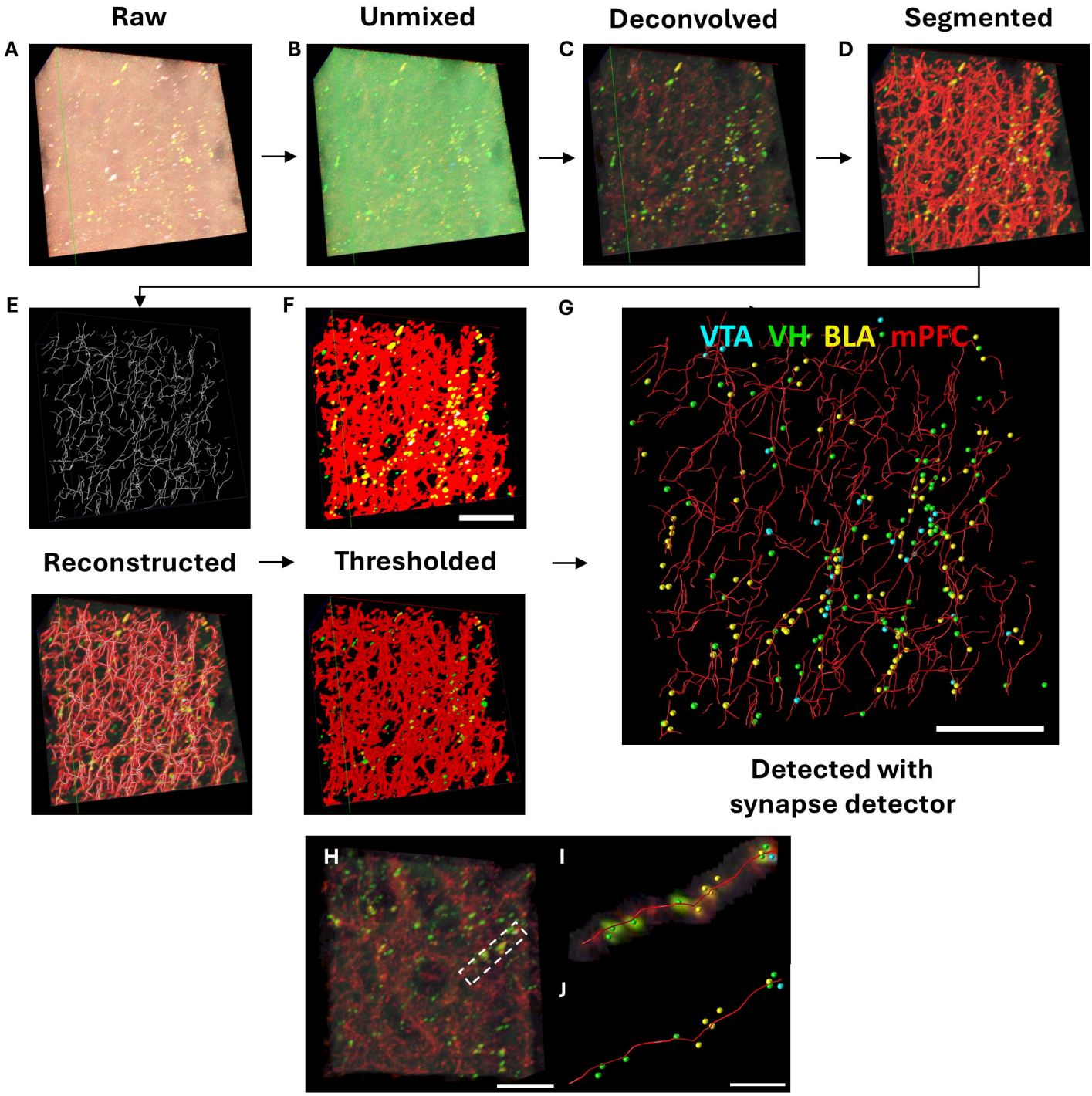
Raw
Unmixed
Deconvolved
Segmented
A
B
C
D
E
F
G
VTA
VH
BLA
mPFC
Reconstructed
Thresholded
Detected with
synapse detector
H
I
J

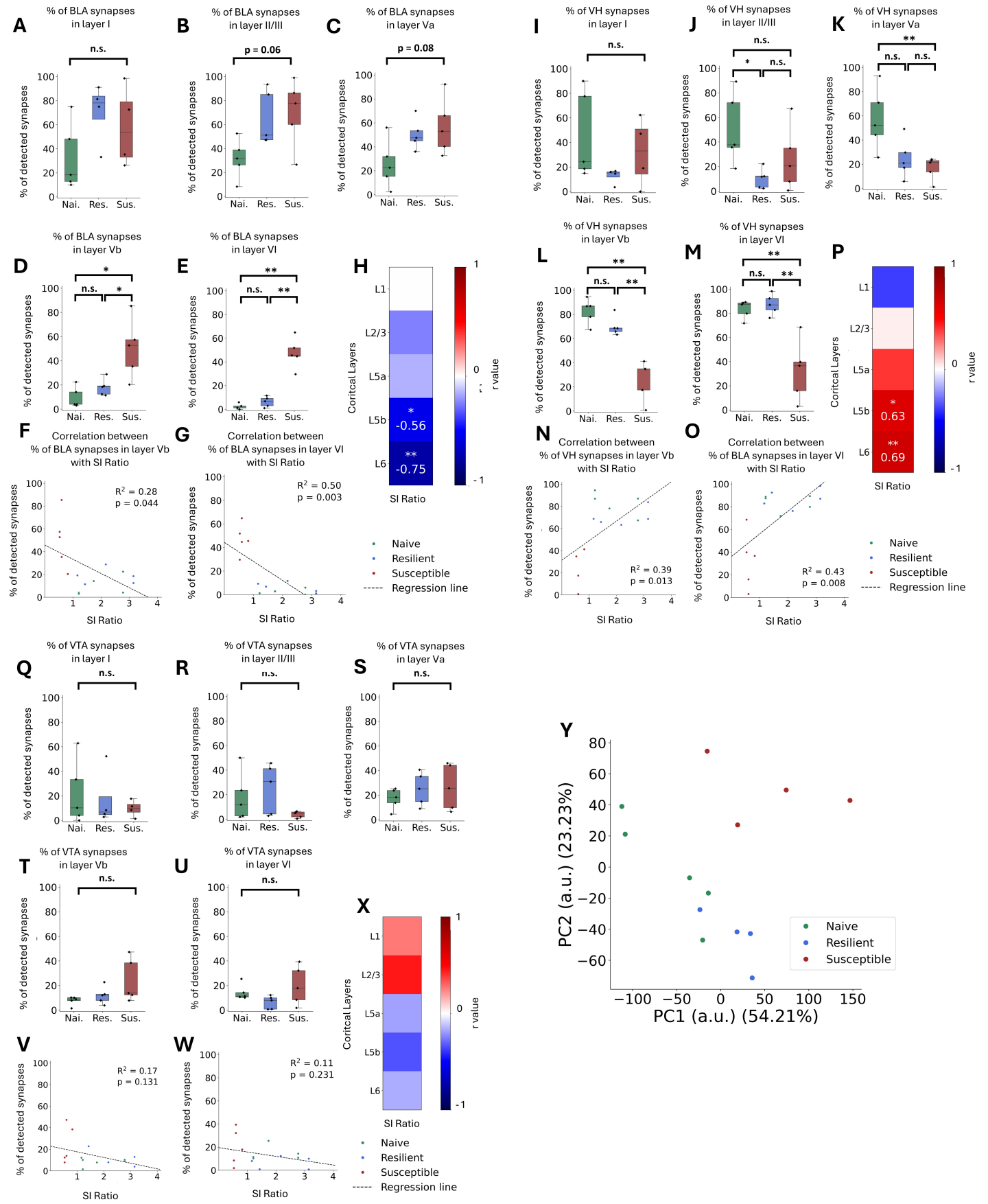
A
% of BLA synapses in layer I
n.s.
B
% of BLA synapses in layer II/III
p = 0.06
C
% of BLA synapses in layer Va
p = 0.08
I
% of VH synapses in layer I
n.s.
J
% of VH synapses in layer II/III
n.s.
*
n.s.
K
% of VH synapses in layer Va
**
n.s.
n.s.
% of detected synapses
Nai.
Res.
Sus.
D
% of BLA synapses in layer Vb
*
n.s.
*
E
% of BLA synapses in layer VI
**
n.s.
**
L
% of VH synapses in layer Vb
**
n.s.
**
M
% of VH synapses in layer VI
**
n.s.
**
H
Coritcal Layers
L1
L2/3
L5a
L5b
L6
*
-0.56
**
-0.75
r value
1
0
-1
P
*
0.63
**
0.69
F
Correlation between % of BLA synapses in layer Vb with SI Ratio
R^2 = 0.28
p = 0.044
G
Correlation between % of BLA synapses in layer VI with SI Ratio
R^2 = 0.50
p = 0.003
N
Correlation between % of VH synapses in layer Vb with SI Ratio
R^2 = 0.39
p = 0.013
O
Correlation between % of BLA synapses in layer VI with SI Ratio
R^2 = 0.43
p = 0.008
SI Ratio
Naive
Resilient
Susceptible
Regression line
Q
% of VTA synapses in layer I
n.s.
R
% of VTA synapses in layer II/III
n.s.
S
% of VTA synapses in layer Va
n.s.
T
% of VTA synapses in layer Vb
n.s.
U
% of VTA synapses in layer VI
n.s.
X
V
R^2 = 0.17
p = 0.131
W
R^2 = 0.11
p = 0.231
Y
PC2 (a.u.) (23.23%)
PC1 (a.u.) (54.21%)

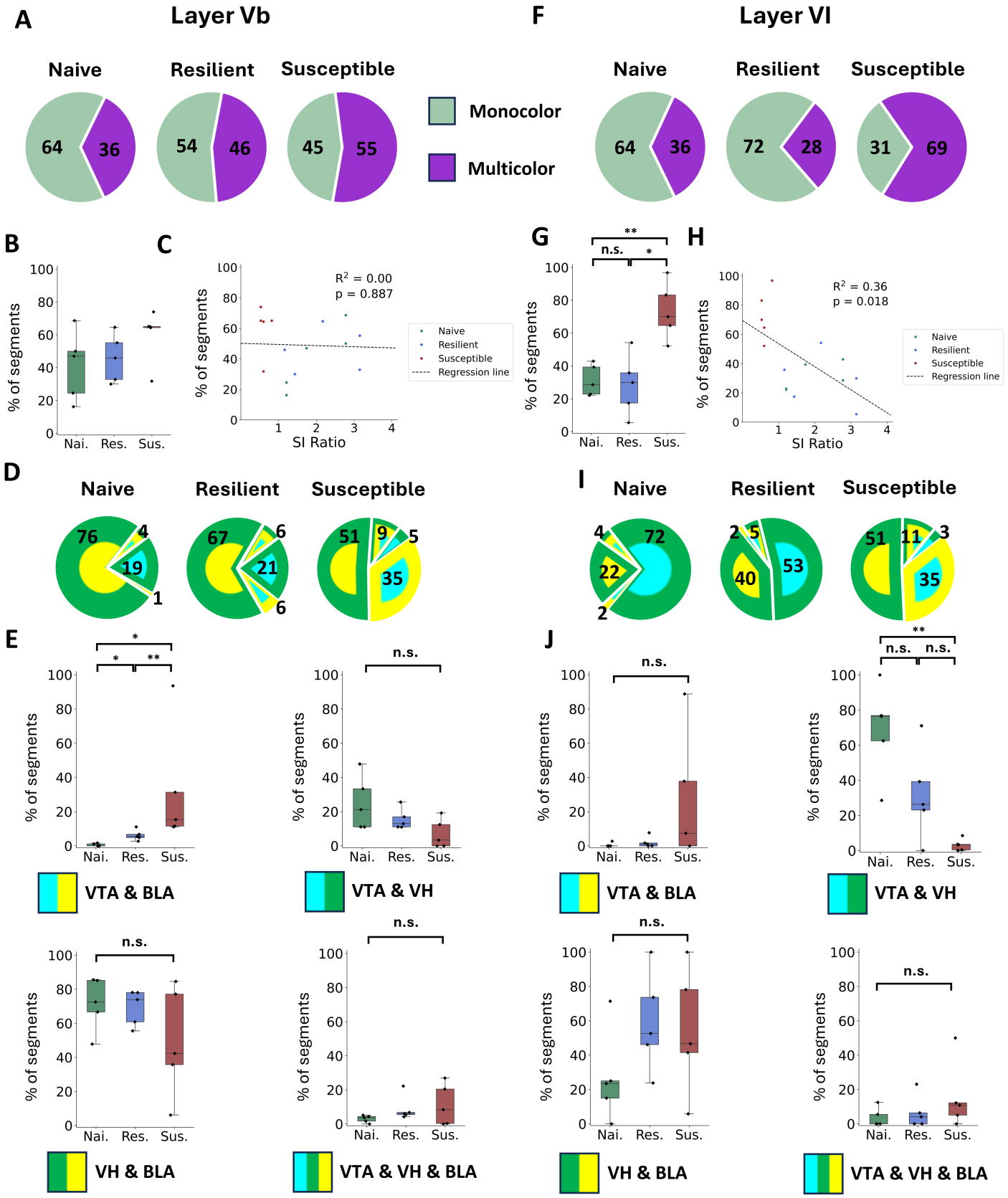
A
Layer Vb
Naive
Resilient
Susceptible
64
36
54
46
45
55
Monocolor
Multicolor
F
Layer VI
Naive
Resilient
Susceptible
64
36
72
28
31
69
B
% of segments
Nai.
Res.
Sus.
C
R² = 0.00
p = 0.887
SI Ratio
Naive
Resilient
Susceptible
Regression line
G
n.s.
*
**
H
R² = 0.36
p = 0.018
D
Naive
Resilient
Susceptible
76
4
19
1
67
6
21
6
51
9
5
35
I
4
72
22
2
2
5
40
53
51
11
3
35
E
VTA & BLA
VTA & VH
VH & BLA
VTA & VH & BLA
J
VTA & BLA
VTA & VH
VH & BLA
VTA & VH & BLA

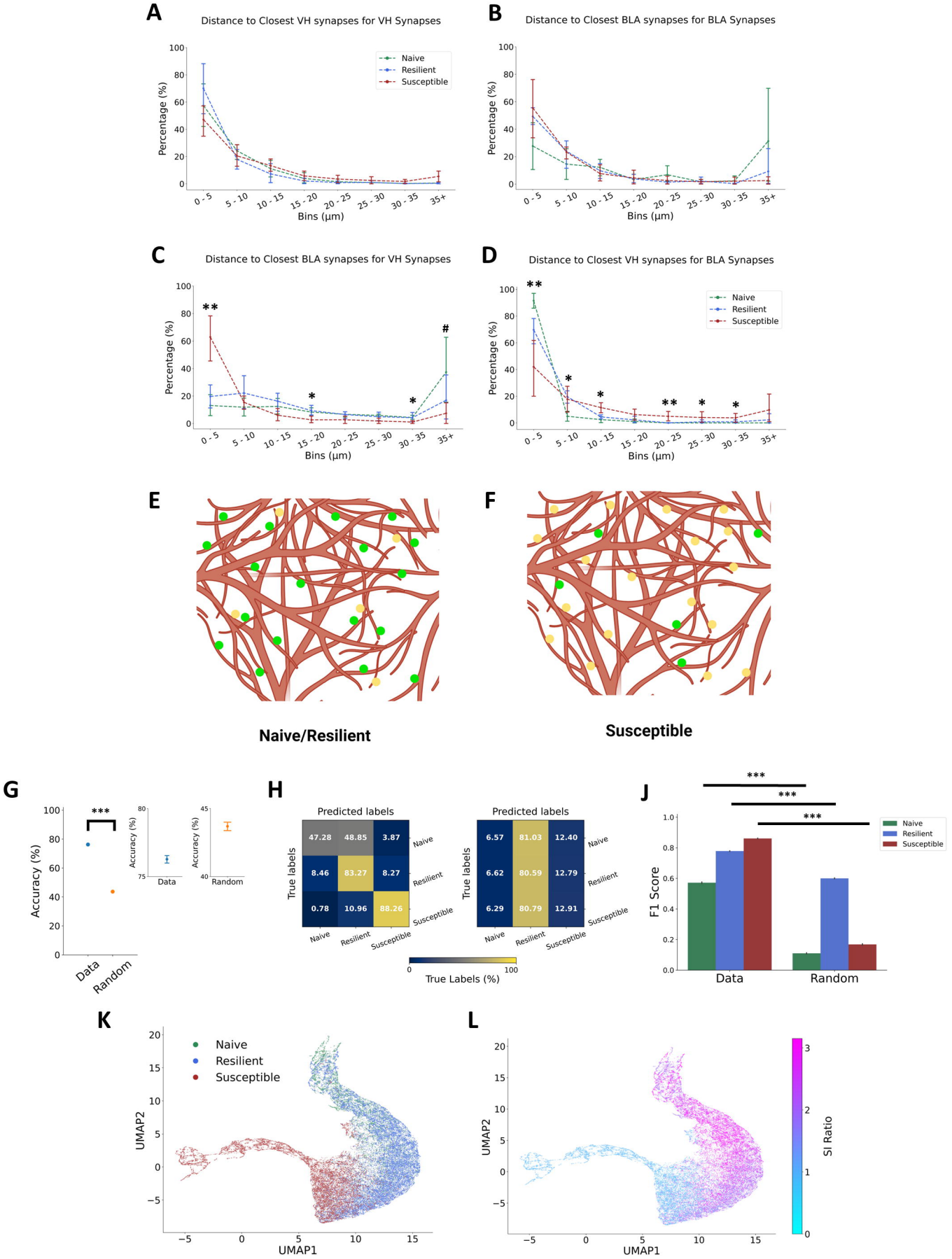
A
Distance to Closest VH synapses for VH Synapses
Percentage (%)
Bins (µm)
0 - 5
5 - 10
10 - 15
15 - 20
20 - 25
25 - 30
30 - 35
35+
Naive
Resilient
Susceptible
B
Distance to Closest BLA synapses for BLA Synapses
C
Distance to Closest BLA synapses for VH Synapses
D
Distance to Closest VH synapses for BLA Synapses
E
F
Naive/Resilient
Susceptible
G
Accuracy (%)
Data
Random
H
Predicted labels
True labels
True Labels (%)
I
F1 Score
J
K
UMAP1
UMAP2
L
SI Ratio